Powder Technology 421 (2023) 118387

Contents lists available at ScienceDirect

Powder Technology

journal homepage: www.journals.elsevier.com/powder-technology

Influence of flake size and electrolyte conditions on graphene oxide adsorption of ionic dyes

James M. Exley[a,*], Timothy N. Hunter[b,*], Thomas Pugh[c], Martin R. Tillotson[a,*]

[a] School of Civil Engineering, University of Leeds, Leeds, West Yorkshire LS2 9JT, United Kingdom
[b] School of Chemical and Process Engineering, University of Leeds, Leeds, West Yorkshire, LS2 9JT, United Kingdom
[c] Evove Limited, Sci-Tech Daresbury, Keckwick Lane, Daresbury WA4 4AB, United Kingdom

HIGHLIGHTS

- Graphene oxides (GOs) of different flake sizes utilised in MB and MO dye adsorption.
- Kinetic and equilibrium studies demonstrated differences between MB and MO sorption.
- GO flake size, charge and surface chemistry all demonstrated to impact adsorption.
- GO flakes aggregated in dye solutions, due to charge neutralisation.
- Divalent salt cations reduced dye adsorption capacities of both GOs in MB.

GRAPHICAL ABSTRACT

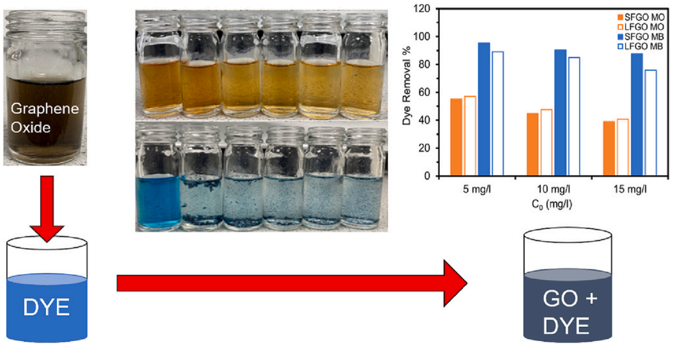

ARTICLE INFO

Keywords:
Graphene oxide
Methylene Blue (MB)
Methyl Orange (MO)
Dye adsorption
Wastewater treatment

ABSTRACT

Two graphene oxide (GO) materials were characterised and their performance as adsorbents for common ionic dyes was investigated. The GOs were demonstrated to possess significantly different flake sizes; here termed Smaller Flake GO (SFGO) and Larger Flake GO (LFGO). Kinetics and isotherm studies using both cationic Methylene Blue (MB) and anionic Methyl Orange (MO) showed adsorption behaviour followed second order kinetics and Langmuir monolayer isotherms in all cases. For MB, adsorption capacities were 526.3 mg/g (SFGO) and 384.6 mg/g (LFGO) with interaction attributed primarily to electrostatic attraction, where the smaller, higher surface area flake led to significantly greater adsorption. In comparison for MO, adsorption was lower at 113.6 mg/g (SFGO) and 149.3 mg/g (LFGO). Here, while electrostatically repulsive, adsorption occurred via π-π interactions and hydrogen bonding, with the LFGO having more favourable surface chemistry. Both GOs were observed to aggregate significantly when dispersed in the dyes, while the introduction of sodium (Na^+) or magnesium (Mg^{2+}) sulphates adversely affected adsorption. For SFGO, MB adsorption reduced by 5.1% (Na^+) and 32.4% (Mg^{2+}). Similarly, for LFGO, MB adsorption capacity reduced by 7% (Na^+) and 17.3% (Mg^{2+}). Adsorption of Mg^{2+} onto vacant binding sites and charge neutralisation were the principal antagonistic mechanisms. These findings demonstrate the potential usage of commercial GO for dye removal and separation and will be of significance to industrial effluent applications.

---

* Corresponding authors.
E-mail addresses: cp17je@leeds.ac.uk (J.M. Exley), t.n.hunter@leeds.ac.uk (T.N. Hunter), m.r.tillotson@leeds.ac.uk (M.R. Tillotson).

https://doi.org/10.1016/j.powtec.2023.118387
Received 5 December 2022; Received in revised form 24 February 2023; Accepted 27 February 2023

1. Introduction

Textile industry dyes are a common source of pollution in surface and ground waters. Many textile industry dyes are known to have adverse effects on public health [1], are capable of causing harm to plant and aquatic species [2], and result in colouration of the water body and connected environment [3]. Examples of common textile dyes include cationic Methylene Blue (MB) and anionic Methyl Orange (MO), which are of comparable molecular weight, and both are known to cause significant health concerns, including heart palpitations and vomiting [4]. Dyes such as these tend to be highly soluble and stable in aqueous solution and are overall difficult to remove using conventional membrane bioreactor treatment systems [5]. These processes tend to have reasonable capacity to reduce chemical oxygen demand (COD) of dye-contaminated waters, however, they often require a subsequent membrane treatment stage to reduce the sludge content [6,7]. Accordingly, existing treatments suffer due to the complexity and necessity for multi-stage operation. Effluent from the textile industry typically comprises dissolved salts in addition to dyes, especially sodium and magnesium salts, which are used in textile processing as dyeing agents [8]. The presence of such salts presents a further complication regarding removal of dyes from contaminated waters, as these may in turn impact upon the treatment process, rendering treatment of textile effluents a challenging problem.

A number of water purification techniques are currently attracting significant research attention in efforts to remove dye contaminants from water. These include adsorption [9], membrane-based separation [10], photochemical oxidation [11] and photocatalytic degradation [12]. Of these techniques, adsorption is a rapid and facile technique to implement, and is one which requires minimal capital investment. Amongst the multitude of existing adsorbent materials, many interesting carbon-based candidates have emerged, including those based on carbon spheres [13] and activated carbon [14]. Two-dimensional (2D) carbonaceous materials [15,16] are promising owing to their high capacity to adsorb dyes from a cocktail of other organic and inorganic micropollutants [17,18].

The emergence of 2D nano-adsorbent graphene oxide (GO) is particularly encouraging. Because of its attributes GO boasts a number of significant advantages as a nano-adsorbent; it has a very high surface area [19], useful mechanical [20] and thermal [21] properties, and favourable surface chemistry and electronic properties [22]. Given its chemistry, GO is by nature a highly functionalisable material. As such, this feature has been employed to generate a great number of modified GO adsorbents, including copper-decorated GO [23] and sulfanilic acid-functionalised magnetic GO [24].

GO may interact with dyes via mechanisms including $\pi-\pi$ stacking [25], electrostatic interaction [26] and hydrogen bonding [27]. The nano-sized structure, sheet-like morphology and electronic properties ensure that interactions with charged species such as certain classes of dyes are plentiful. GO possesses an overall negative charge, owing to the decoration of the sheet edges with an array of oxygen-containing functional groups such as hydroxyl ($-OH$), carboxyl ($-COOH$) and epoxy ($-COC-$) groups [28,29]. In solution, hydrogen atoms deprotonate from these groups, thus imparting an overall negative charge [30]. In terms of adsorption processes, such properties enable GO to yield a high dye adsorption capacity, but present a significant challenge associated with usage of the material as an adsorbent i.e. irreversible aggregation of GO layers [31]. Aggregation of GO layers is particularly prominent if cations or cationic dyes are introduced, as these species can neutralise the GO charge, therefore mitigating the effects of electrostatic repulsion [32]. This change may hinder the potential recyclability of the adsorbent, thus necessitating the development of a means for cost-effective and facile regeneration [33]. Recycling has thus far proven a challenging task, though an example of progress is the sponge-like GO material of Sun et al. [34], in which the adsorbed dye was removed by squeezing, and the recycled GO washed in sodium hydroxide prior to reuse.

Despite these limitations, studies of unmodified GO, particularly in the adsorption of MB, have been widely reported. Early research by Sharma and Das [35] focussed on the utility of GO prepared from graphite powder by the Hummers' Method [36]. Kinetics studies conducted in the temperature range 18–35 °C showed GO was able to adsorb MB with high capacity (1.4 mmol/g). Yan et al. [37] also studied GO produced from the Hummers' Method, and reported that an intentional increase in the degree of oxygen functionalisation resulted in high MB adsorption capacity (598.8 mg/g). Arias Arias et al. [38] discussed adsorption of MB utilising eco-friendly GO from a graphite powder using an in-house synthesis and purification method, but the adsorption capacity for MB appeared somewhat lower (68.8 mg/g), possibly due to the particulars of the experimental methods, including such factors as pH.

A trend that appears consistent in the literature is the popularity of GO synthesis from graphite powder by laboratory methods such as the Hummers' Method. The utility of commercial GO products, that require minimal or no additional synthesis or purification stages prior to use, appear comparatively under-reported. One example of commercial GO application in a dye adsorption system was reported by Zhang et al. [39], who employed a commercial GO for adsorption of MB, achieving a highly encouraging adsorption capacity (429 mg/g). It thus appears that commercial GO materials are promising candidates for the adsorption of dyes yet, despite this, they have been under-utilised in research. Commercial GO appears to have a number of advantages compared to laboratory prepared GO for dye adsorption applications. These include reliability of formulation, time-savings, experimental and performance reproducibility, and better potential for scaleup, all of which lend themselves to upscale industrial applications. For the aforementioned reasons, commercial organisations may therefore be expected to favour commercial GO sources over synthetically prepared ones. To the best of our knowledge, however, no published work exists comparing the efficacy of a number of commercially available GO products as dye adsorbents. We consider such a need to be timely, as it enables commercial and industrial entities to expand their knowledge of GO nano-adsorbents tailored to specific applications as the research field starts to mature. It is anticipated that the scale-up potential of the GO adsorbents within the treatment of dye contaminations will lead to widespread adoption of the technologies as competitors for alternative methods such as those suggested above, including membrane treatments.

In this article, we report a detailed investigation regarding the capabilities of two commercially available GO dispersions as dye adsorbents in the removal of anionic MO and cationic MB dyes in water. The opposite charges of the two dyes allowed for studies into the role of GO surface charge on adsorption affinity. We also extended our understanding on binary GO–dye adsorption by dissolving sodium and magnesium sulphate salts into MB dye systems prior to injection of GO adsorbent, thus allowing exploration of the impact of external charged species on dye adsorption processes. Aggregation phenomena of GO in MB and MO was also investigated, as this remains a major scientific obstacle regarding the application of GO as an adsorbent in aqueous systems.

2. Experimental

2.1. Materials

Graphene Oxides were obtained from two commercial suppliers as 1.0 wt% dispersions in water. Due to commercial sensitivity, we are not able to disclose the source of the graphene oxide materials described in this study, or any details on supplying companies. Aqueous anionic Methyl Orange (MO, at a supplied solution concentration of 0.10 wt%) and cationic Methylene Blue (MB, at 0.50 wt%) dyes were obtained from Merck (Germany). Sodium sulphate ($Na_2SO_4 \bullet 10H_2O$) and magnesium sulphate ($MgSO_4 \bullet 7H_2O$) were also obtained from Merck (Germany). All chemical reagents and solvents were used without further purification or modification.

2.2. Characterisation of GO materials

Fourier Transform Infrared (FTIR) spectroscopic analysis was performed using a PerkinElmer (USA) spectrophotometer. The aqueous GO dispersions were oven dried overnight onto glass slides, and the powdered GO extracted by scraping the dried material from the slides and crushing using a mortar and pestle. 5 mg of GO powder was then mixed with 300 mg spectroscopic grade KBr and crushed into a fine, uniform powder using a mortar and pestle. The GO-KBr mixture was compacted into a thin disk using a hydraulic press, before FTIR analysis was performed in transmission mode and completed with 32 scans in wavenumber interval 4000–400 cm^{-1}.

Raman Spectroscopy was carried out using a Horiba XploRA PLUS (Japan) fitted with a 100× objective lens. Aqueous dispersions of 1 wt% GO were dried overnight on glass slides in a sealed oven. The wavelength of the incident excitation laser was 532 nm, with power output 1.2 mW. The intensity of the Raman Shift was recorded in the wavenumber range 3000–500 cm^{-1}. One measurement site was chosen for each sample.

X-Ray Diffraction (XRD) analysis was performed using a Bruker D8 (USA) diffractometer, with CuK_{α} radiation source (wavelength 0.154 nm, 40 keV, 30 mA). For XRD analysis, powdered GO samples were prepared as per the method used for FTIR analysis (above). The powdered samples were placed inside a single silicon crystal holder for analysis. XRD instrumentation settings were: angular scan range $5^0 < 2\theta < 50^0$, incremental step size 0.016 degree/min, step interval 0.40 s/step. The total scan time required for analysis of each sample was 30 min.

X-Ray Photoelectron Spectroscopy (XPS) survey and high resolution O 1s and C 1s analysis was carried out using a Thermo Fisher Scientific Escalab 250Xi (USA) ultrahigh vacuum XPS instrument (AlK_{α} X-ray emission source). Photoelectron pass energy for survey spectra was 40 eV and for high-resolution C 1s and O 1s spectra 20 eV. XPS data was processed using CASAXPS software with adventitious carbon (284.6 eV) as the reference peak. For high-resolution C 1s and O 1s scans, smoothing of raw experimental data was achieved using the software's in-built quadratic smoothing tool. Background correction was achieved using a Shirley background function [40]. Deconvolution of spectra was performed using peak fitting with Gaussian-Lorentzian shapes [41].

Brauner-Emmett-Teller (BET) surface analysis was carried out using a Micrometrics Tristar 3000 (USA). The mass of powdered GO used for testing was recorded as 10 mg. Degassing of samples was achieved by transferring the powders into a round-bottomed flask and purging with Nitrogen in a Micrometrics FlowPrep (USA). The samples in flasks were then attached to the surface area analyser, and liquid nitrogen at 77 K was decanted into the Dewar flask prior to lowering of the samples.

Dynamic light scattering (DLS) analysis, including particle sizing and analysis of zeta potential, was carried out using a Malvern Panalytical Zetasizer (UK). Analysis was conducted in folded capillary zeta cells. Aqueous 1 wt% GO samples were diluted to 0.01 mg/ml in distilled water. Adjustment of pH to the interval 3.5–10.0 was achieved using dilute 0.10 mol/dm^3 NaOH. For zeta potential measurements of salt-in-GO colloids, sodium and magnesium sulphates were dispersed into dilute GO at the respective concentrations 0, 1, 2, 4, 6, 8, 10 g/l.

Laser diffraction (LD) particle size analysis was carried out using a Malvern Panalytical Mastersizer 3000 (UK). Analogous to DLS analysis, aqueous 1 wt% GO samples were diluted to 0.01 mg/ml in distilled water prior to pouring approximately 20 ml of dilute sample into the wet sample chamber.

2.3. Adsorption of dyes using GO adsorbents

2.3.1. Kinetics of dye adsorption

For adsorption of MB, 5 mg of GO from the original 1 wt% dispersion was transferred by pipette into 100 ml of prepared dye solution, such that the weight by volume ratio of GO to water was 0.00498 *w*/*v*%. The GO-MB mixture was constantly agitated during the adsorption procedure using a magnetic stirrer bar at speed setting 5 on the stirrer. The UV absorbance of the dye was measured at the beginning of the experiment using a Thermo Fisher Scientific Biomate 3 (USA). A total of three dye concentrations were used in these experiments (5, 10 and 15 mg/l). 5 ml aliquots of the GO-MB suspension were withdrawn at times of 10, 20, 30, 40 and 50 min after transfer, and centrifuged at 4000 rpm using an Eppendorf Centrifuge 5810 (Germany) for ten minutes in order to separate the GO from the MB. The supernatant MB was filtered through a Sartorius Minisart Syringe Filter Plus (Germany) 0.45 μm cellulose acetate syringe filter, and UV absorbance was measured. It is noted that the UV calibration curves for both MB and MO dyes are given within the Electronic Supplementary Materials (ESM) for completeness (see Fig. S1). All dye experiments were all conducted at pH 7, in line with expected wastewater conditions.

For adsorption of MO, the above method was adjusted owing to the more limited adsorption of MO by the GO's. The dosage of GO was set at 10 mg for each experiment, such that the volume ratio of GO to water was 0.00990 *w*/*v*%. The GO was observed to be slower at dropping out of the GO-MO suspension and, as such, the centrifugation time was increased from 10 min to 25 min.

Dye adsorption at time *t* (minutes), denoted as q_t (mg/g), and the equilibrium dye adsorption, q_e (mg/g), are given by Eqs. (1) and (2), respectively:

$$q_t = (C_0 - C_t)/(m^* V) \tag{1}$$

$$q_e = (C_0 - C_e)/(m^* V) \tag{2}$$

where C_0, C_t and C_e are the concentrations of dye (mg/l) at initial stage (time zero), time *t*, and the equilibrium stage, respectively. Additionally, *V* is the total volume of solution (litres); and *m* is the mass of adsorbent (grams). It is assumed during the analysis that the volume of solution is unaltered by the adsorption of dye onto GO, thus the value of *V* is taken as constant throughout the adsorption process.

The dye removal percentage was calculated according to Eq. (3):

$$\text{Removal }(\%) = ((C_0 - C_e)/C_0)\cdot 100\% \tag{3}$$

For experiments concerning the effects of salt addition upon dye adsorption kinetics, MB was selected as the probe dye. Sodium sulphate and magnesium sulphate were dispersed into 15 mg/l MB solutions of 100 ml volume using the same mixing procedure as above. The salt loadings chosen for these experiments were 50, 100, 150 or 200 mg. GO loadings were 5 mg, consistent with above, such that the volume ratio of GO to water was 0.00498 *w*/*v*%. The kinetics of dye adsorption were monitored in an analogous fashion to the case for which there was no salt added to the dye.

2.3.2. Kinetic models

To analyse the data obtained in the kinetics of dye adsorption studies, two linearised models were used; pseudo-first order (PFO) and the pseudo-second order (PSO) rate models [42,43].

The PFO model is given by Eq. (4):

$$ln\left(q_{e,exp} - q_t\right) = -k_1 \cdot t + ln\left(q_{e,cal1}\right) \tag{4}$$

where k_1 is the first order adsorption rate constant (min^{-1}), $q_{e,cal1}$ and $q_{e,exp}$ are the respective values for first order calculated q_e and experimental q_e (units consistent with definition of q_e, above). In PFO analysis, a plot of $ln(q_{e,exp} - q_t)$ versus *t* therefore yields the values of k_1 and $q_{e,cal1}$ from the gradient and vertical intercept, respectively.

The PSO model is given by Eq. (5):

$$t/q_t = t/q_{e,cal2} + 1/\left(k_2^*\left(q_{e,cal2}\right)^2\right) \tag{5}$$

where k_2 is the second order adsorption rate constant (g/(min·mg)) and $q_{e,cal2}$ is the second order calculated q_e. A plot of t/q_t versus t thus enables the values of $q_{e,cal2}$ and k_2 to be extracted from the gradient and vertical intercept, respectively.

2.3.3. Equilibrium of dye adsorption

Experiments to understand the equilibrium of dye adsorption were carried out using 20 mg GO adsorbent for MB studies and 30 mg GO for MO studies. The adsorbent was dispersed and agitated in 100 ml dye solution at an initial concentration range of 50, 75, 100, 125 and 150 mg/l. The respective volume ratio of GO to water was 0.0196 *w*/*v*% for MB and 0.0291 w/v% for MO. 5 ml of the GO-dye suspension was extracted at a time 80 min after addition of adsorbent, centrifuged, and the filtered supernatant analysed by UV spectrophotometry as previously described.

2.3.4. Equilibrium isotherm models

The adsorption of one species onto another is a dynamic process, and if the interaction proceeds for a sufficient length of time, an equilibrium will be established between the amount of adsorbate in solution and the amount adsorbed [44]. This relationship is quantifiable by means of an adsorption isotherm: a formal means of relating concentration of a species on the surface of an adsorbent to the concentration of that species in solution at equilibrium. Two equilibrium isotherms were considered in this study, those of Freundlich and Langmuir.

The Freundlich isotherm model considers heterogeneous adsorption onto an adsorbent surface. The governing linearised equation is given by Eq. (6) [45]:

$$ln(q_e) = 1/n^{*} ln(C_e) + ln(K_F) \tag{6}$$

where K_F is the Freundlich constant $((\text{mg}\cdot\text{g})\cdot(\text{l}\cdot\text{g}))^{1/\text{n}}$, and n represents the deviation from linearity. A plot of $ln(q_e)$ versus $ln(C_e)$ will be linear if the Freundlich model is obeyed, with slope equal to the reciprocal value of n and the intercept equal to $ln(K_F)$. The Langmuir isotherm model assumes monolayer coverage of an adsorbate over a homogeneous surface of adsorbent. According to Langmuir, the adsorbate may bind to all available sites on the adsorbent surface with equal probability, and each site can hold at most one molecule [46]. The linearised version of the Langmuir model is defined mathematically by Eq. (7) [47].

$$C_e/q_e = 1/(K_L{}^{*} q_{max}) + C_e/q_{max} \tag{7}$$

where K_L is the Langmuir constant (l/g), and q_{max} (mg/g) is the maximum adsorption capacity. A plot of C_e/q_e versus C_e ought to reveal a linear relationship with a gradient equal to $1/q_{max}$ and the vertical intercept $1/(K_L{}^{*}q_{max})$ which enables q_{max} and K_L to be extracted from the intercept and gradient, respectively.

In Langmuir analysis, the dimensionless R_L parameter is also used to indicate favourability of adsorption: if $R_L > 1$ the process is unfavourable, if $R_L = 0$ the process is irreversible and if $1 > R_L > 0$ then the process is favourable [38,46,48]. R_L is defined by Eq. (8).

$$R_L = 1/(C_0{}^{*} K_L) \tag{8}$$

3. Results and discussion

3.1. Characterisation of GO materials

Particle size distributions (PSDs) obtained by LD and DLS are shown in Figs. S2a and S2b of the Electronic Supplementary Materials (ESM), respectively. A summary of the results of BET, LD and DLS analysis of the two GOs (denoted Type 1 and Type 2) are shown in Table 1:

Cursory inspection of the *Z*-Mean and d(50) results reveals the Type 1 GO is typically of the order of one magnitude smaller in size than Type 2. Hence, throughout the article, they will henceforth be referred to as 'smaller flake' GO (SFGO) and 'larger flake' GO (LFGO), respectively.

Perhaps more notable is the large discrepancy in size values calculated by the two laser based techniques. In terms of particle size range suitability, DLS is limited to analysis of particles which are maximally 10^0–10^1 μm in size, as it is a diffusion limited technique, whereas LD covers a range of up to 10^3 μm. Given that the d(50) and modal peak values of SFGO and LFGO were of the order 10^1 *μ*m and 10^2 μm, respectively, it appears LD is the more suitable analytical technique. DLS and LD also differ in their approximations for large aspect ratio particles [49], such as those expected with GO flakes. DLS measurements are based on approximating diffusion to spherical equivalent hydrodynamic diameters, while scattering intensity from laser diffraction is more aligned to the maximum axis length (assuming random orientation in the measurement cell), thus accounting for the large discrepancies between the respective LD and DLS sizes [50]. Additionally, BET analysis revealed SFGO has a far higher specific surface area than LFGO, correlating to the smaller flake sizes resulting in higher surface area:volume ratios of the sheets. Comparison of GO size results with those available in the literature suggests the sizes obtained by LD are consistent [51,52].

FTIR analysis enables identification of functional groups present within a material. The results of FTIR analysis for SFGO and LFGO powders are shown in Fig. 1a. The gross similarity of the spectra suggests that the functional groups present within the materials are similar. SFGO and LFGO both exhibit a peak at approximately 3430 cm^{-1}, which is attributed to an –OH hydroxylic stretch [53], while bands at 1730 cm^{-1} and 1630 cm^{-1} are indicative of C=O (carboxylic acid) stretch, and C=C (carbon double bond) stretching, respectively [54]. Further peaks observed in the materials at 1100 cm^{-1} and 1070 cm^{-1} are indicative of vibrational stretching of C—O and C—C groups [55].

The XRD patterns of SFGO and LFGO are shown in Fig. 1b, with the samples having a characteristic peak located at $2\theta = 11.34^0$ and 11.09^0, respectively. By the Bragg Eq. [56], these peaks correspond to calculated (001) crystal plane interlayer spacing of 0.780 and 0.798 nm for SFGO and LFGO, respectively. The broad shape of the dominant (0 0 1) peaks indicate both materials have low crystallinity [57]. These peaks and d-spacings are consistent with those reported elsewhere in the literature for graphene oxide materials [53,58–60]. The interlayer spacings of GO materials measured by XRD are typically larger than those observed in alternative materials such as graphite, owing to the insertion of oxygen functionality at the edges of the sheets thus increasing interlayer electrostatic repulsion and contributing to the separation of layers [61]. The slightly larger d-spacing observed for LFGO compared to SFGO may be attributed to the particular arrangement of the oxygen containing functional groups present within the sheets [57]. Both SFGO and LFGO exhibit a secondary, relatively lower magnitude peak at $2\theta = 42.5^0$ and 42.4^0, respectively. This is a common feature of GO materials, and it has been proposed that the occurrence of these secondary peaks is due to the presence of unexfoliated, stacked layers of GO [62].

Raman spectra of SFGO and LFGO are shown in Fig. 1c. Raman spectra of a graphitic material consists of two dominant peaks, commonly denoted D and G peaks, occurring at Raman Shift values of approximately 1350 and 1600 cm^{-1}, respectively. The presence of a G peak is indicative of first order scattering of the E_{2g} phonon in carbon–carbon bonds; as such is common to all graphene-based materials [63]. The D peak is rather more commonly associated with GO materials, as it has arisen from inherent structural defects within the material [64]. The introduction of oxygen containing groups in GO creates an abundance of

Table 1
BET, DLS and LD analysis of Type 1 and Type 2 GOs.

	$S_{BET\ (m\ g)}^{2}$	DLS z-mean (*μ*m)	LD d(10) (*μ*m)	LD d(50) (*μ*m)	LD d(90) (*μ*m)
Type 1 (SFGO)	85.4	0.4	4.4	9.0	18.8
Type 2 (LFGO)	23.2	1.6	3.5	13.6	29.7

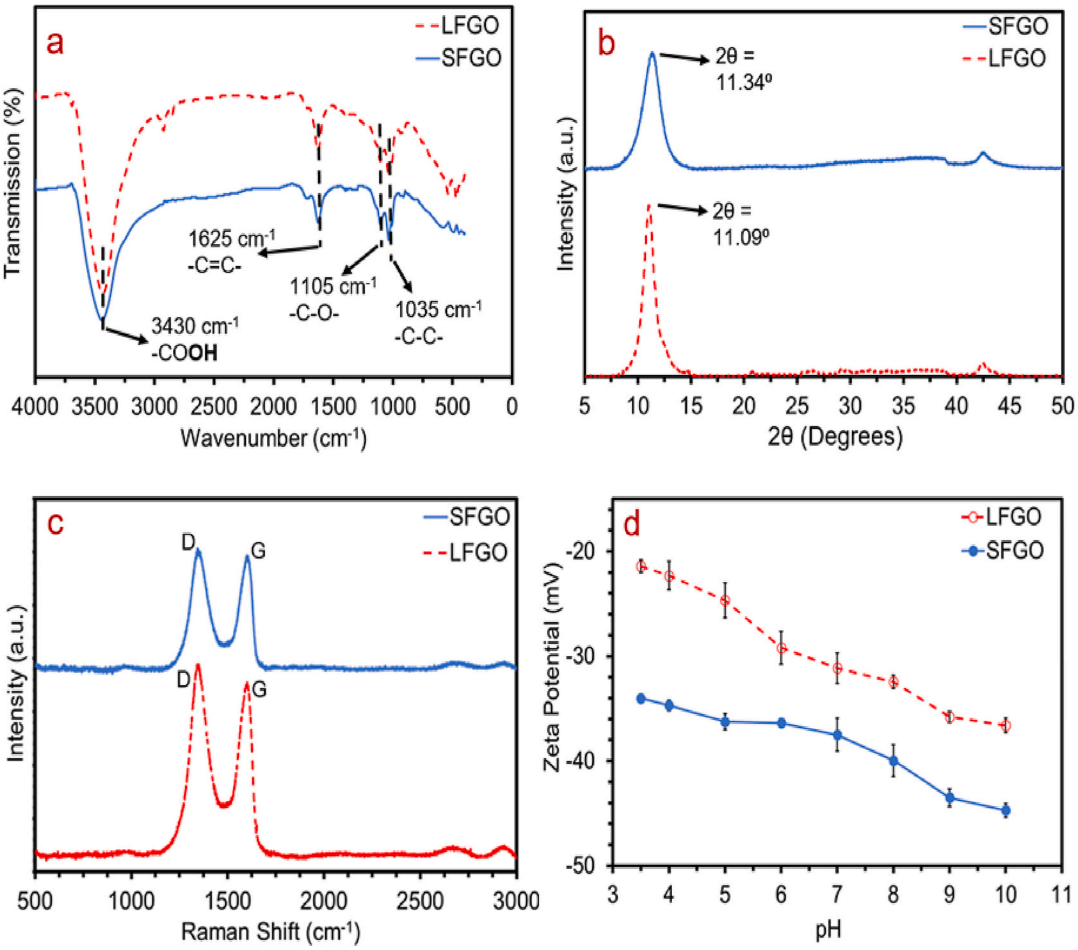

Fig. 1. Analysis of SFGO and LFGO by a) FTIR, b) XRD, c) Raman Spectroscopy and d) Zeta Potential measurement.

defects in the structure due to imperfect oxidation of the material, and this enhances the Raman scattering effects, resulting in the emergence of the D peak [65]. Magnitude ratios of the D and G peaks, denoted I_D:I_G, is a commonly used indicator of the level of disorder within a graphitic material structure. Calculated I_D:I_G ratios for SFGO and LFGO were markedly similar at 1.08 and 1.10, respectively. Such values are typical of GO [66,67]. For GO materials, it is common for the I_D:I_G ratio to be approximately or even exceeding unity; a feature resulting from the breakage of sp^2 carbon–carbon bonds and formation of new sp^3 bonds upon the insertion of oxygen and carbon–oxygen bonding [68–70].

The zeta potential, measured as a function of dispersion pH, for 0.01 mg/ml SFGO and LFGO are shown in Fig. 1d. The zeta potential is an electro-kinetic phenomenon, defined as the electric potential difference between the slipping plane around a suspended particle and an arbitrary point in the bulk phase of the medium [71]. It is often used to qualitatively indicate the colloidal stability of a dispersion. The SFGO and LFGO are shown to exhibit increasing stability (decreasing zeta potential) subject to increasing pH in the range 3.5–10.0. The SFGO exhibits, on average, the largest peak zeta potential across the complete pH range, and has the highest potential value of −44.7 mV at pH 10.0, compared to that of LFGO, which exhibits its greatest magnitude value of −34.9 mV at pH 10.0. The high negative zeta potential magnitudes of both GOs suggest they will be relatively electrostatically stable in water, thus resisting aggregation. These findings correspond to similar observations in previous research [72,73]. In addition, and owing to the electronegative charges, both GOs will be more likely to adsorb the cationic MB dye as a result of electrostatic attraction. The greater magnitude of the SFGO may suggest stronger electrostatic attraction with MB will occur, potentially leading to differences in adsorbed amounts.

XPS analysis is used for qualitative and quantitative identification and analysis of atomic species and functional groups present within the outer 10 nm of a material [74]. Survey spectra were used to detect the presence and quantity of atomic species; these are given in Fig. S3 of the ESM. The survey scans indicated the presence of two peaks, present at photoelectron binding energies of 532.0 eV and 286.0 eV, confirming the presence of oxygen and carbon, respectively. Atomic percentages of the SFGO and LFGO samples were as follows: SFGO – 74.4% carbon, 25.6% oxygen, LFGO – 71.9% carbon, 28.1% oxygen. The slightly higher oxygen content of the LFGO sample is consistent with the larger d-spacing, obtained during XRD, as the overall greater percentage of oxygen results in a greater degree of electrostatic repulsion of the sheets [75].

High resolution C 1 s spectra for SFGO and LFGO are shown in Fig. 2a and b, respectively. Both spectra were deconvoluted to five peaks in total, with the identity of the peaks provided by [76–78]. Both GOs possessed peaks associated with a number of functional groups which were also observed in our FTIR analyses, these include –C–O– (286.5 eV), –C–C– (285.5 eV), –COOH (289.3 eV), –C=O (287.5 eV) and C—C (284.6 eV). Deconvolution of the high resolution O1s spectra for SFGO (Fig. 2c) and LFGO (Fig. 2d) yielded four peaks for both materials, with the identities referring to [79–81]. Again, a number of these deconvoluted peaks may be associated with functional groups which were observed in the FTIR spectra, for example –C–O– (533.3 eV) and –C=O (530.5 eV). Both materials were also found to possess a peak at 532.0 eV corresponding to –C–O–C– groups. The spectra also revealed the presence of a trace peak at 535.5 eV, associated with residual moisture due to incomplete drying of the materials prior to analysis.

Using XPS in conjunction with FTIR analyses has provided a means to

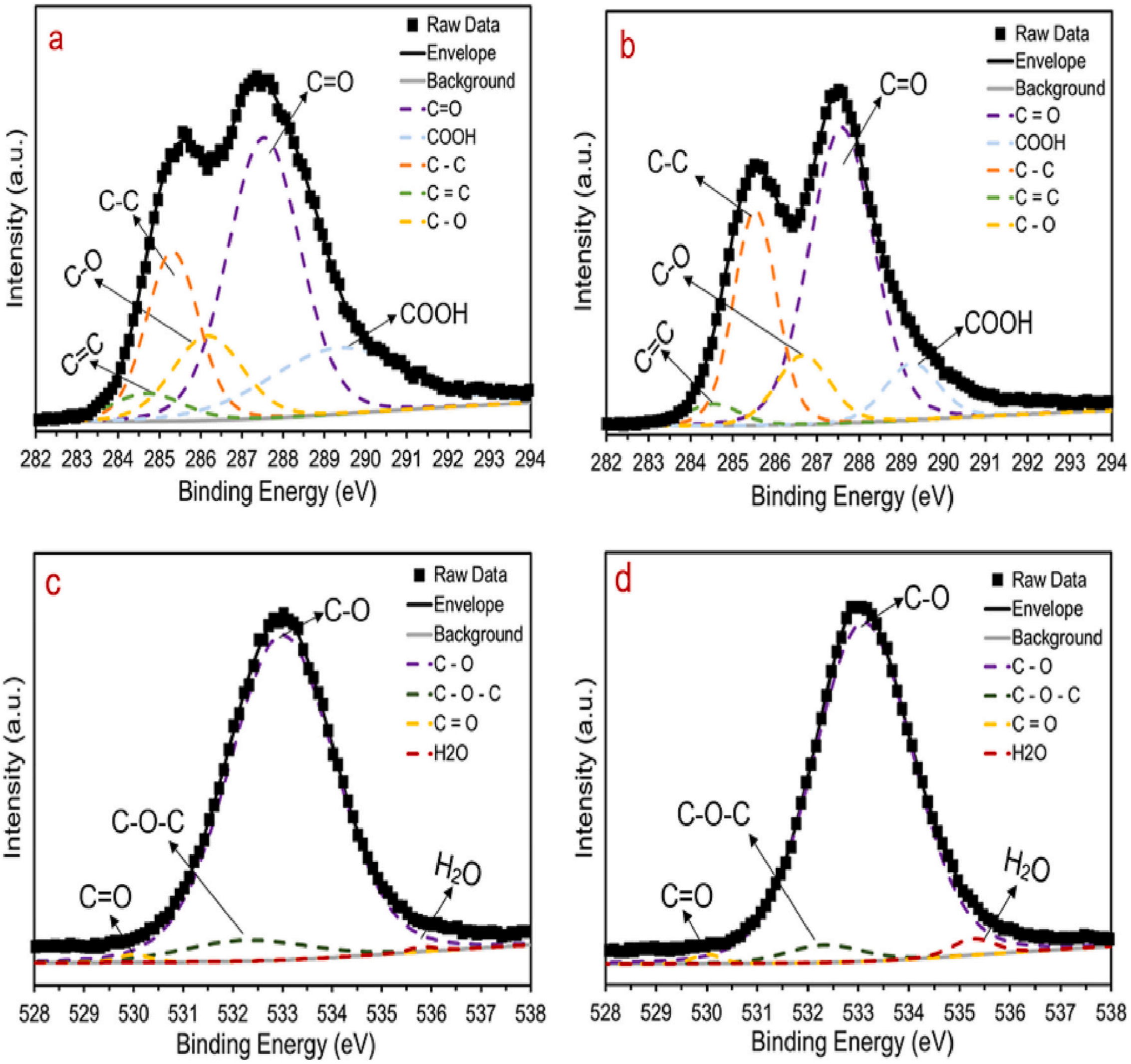

Fig. 2. *XPS analysis of SFGO and LFGO, showing high resolution C 1 s spectra of a) SFGO and b) LFGO; and high resolution O 1 s spectra of c) SFGO and d) LFGO.* Spectra were collected at a single point per sample.

evaluate the chemical nature of the commercial GO materials. There were evidently a plethora of functionalised carbon- and oxygen-containing groups present on the surfaces. Additionally, our analyses revealed both SFGO and LFGO possess a particular number of functional groups which enable chemical interactions with MB in dye adsorption processes, such as the oxygen-rich –C–O–, –COOH and –C=O groups [82]. Recent molecular dynamics simulations by Dhar et al. [83] have demonstrated that the interaction between MB and GO is dominated by the surface chemistry of the GO and, in particular, the oxygen-containing groups on the GO adsorbent surface. The presence of these groups in the outermost layers, as confirmed by XPS, promotes interaction and leads to favourable outcomes in dye adsorption. Perhaps the most significant overall difference in chemistry between the two samples is the slight difference in oxygen content, as discussed above, the LFGO sample has a higher degree of oxygenation relative to SFGO. A higher oxygen content of GO materials has been correlated to greater adsorption capacity for cationic dyes [84]. In the subsequent chapters, however, will demonstrate that this is not observed in our systems, implying that other features may also be responsible for the behaviour. XPS has also been utilised to confirm the adsorption of MB on Fe_3O_4@SiO_2@CS-TETA-GO nanoadsorbents, in research by Wang et al. [85] (and in their earlier work [86]) in which a new peak, corresponding to S 2p presence, was identified post-adsorption of the dye. In addition, quantitative analysis of the O 1 s and N 1 s bonding in high resolution spectra revealed that the quantities of functional groups changed due to the adsorption of MB.

3.2. Dye adsorption

3.2.1. Kinetics of dye adsorption

Understanding dye adsorption kinetics is an important step in the analysis of adsorbent-adsorbate systems. Calculated values of q_t as a function of time for the SFGO and LFGO are presented for MB adsorption (Fig. 3a) and MO adsorption (Fig. 3b), with fitted pseudo-second order (PSO) kinetics profiles for each. The linear pseudo first order (PFO) and PSO plots are shown in Figs. S4 and S5, within the ESM. The standard deviational error in value of q_t calculated across three experimental runs is tabulated in Table S1 within the ESM, for dye concentrations 5, 10 and 15 mg/l.

Example images of the GO-dye dispersions are given in Fig. 3c and 3d for MB and MO dyes respectively, over the 50 min adsorption period (prior to centrifugation of the GO-dye dispersions). By inspection, these images reveal that the respective blue and orange colouration of MB and MO decreases subject to an increase in contact time. Additionally, in the case of MB in particular, it is evident that aggregation of GO in the dye is taking place, as large, clustered sections of flake-like matter are clearly visible. Aggregation of GO with dye will be considered in more detail within Section 3.2.3.

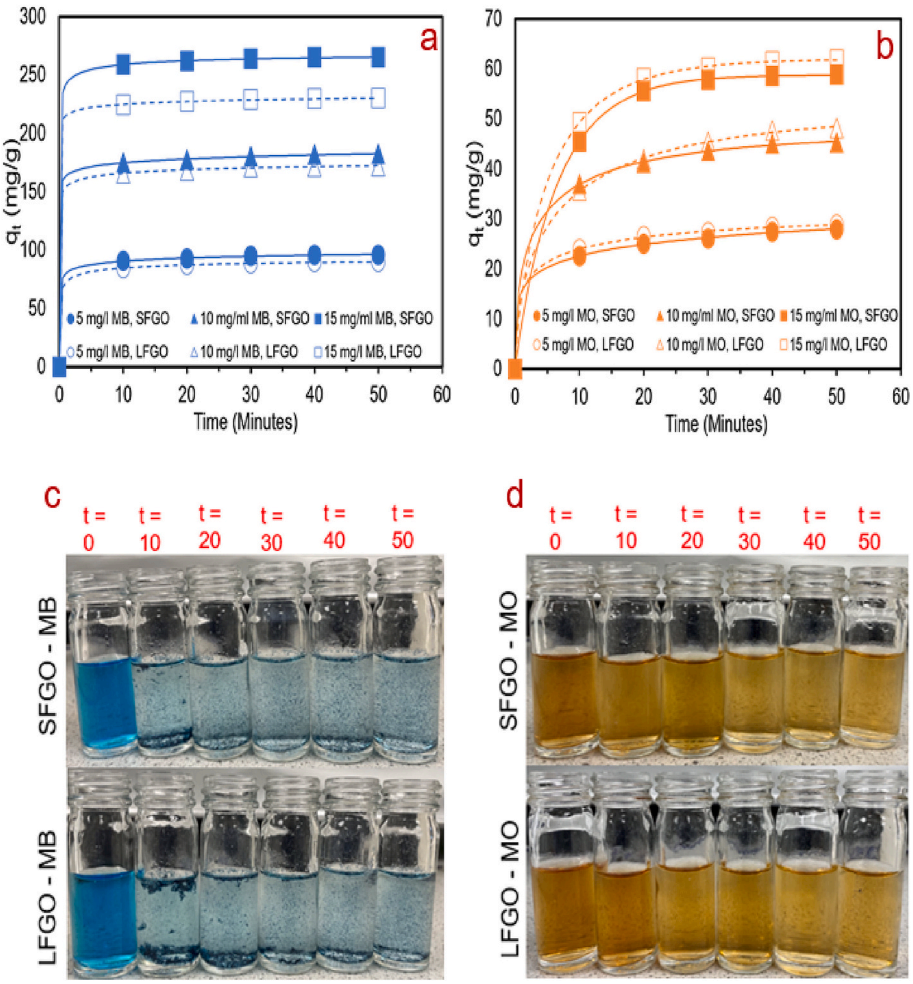

Fig. 3. Kinetic q_t versus contact time for a) MB adsorption, and b) MO adsorption, with both dyes at initial concentration 5, 10 or 15 mg/l. For MB samples, GO loading was 5 mg. Standard deviation in q_t is given in Table S1 of the ESM. Images showing adsorption of c) MB by SFGO and LFGO at t = 0–50 min., and d) MO by SFGO and LFGO, at t = 0–50 min. The samples of dye chosen for these images were at initial concentration 10 mg/l.

The adsorption of MB appears to take place rapidly, with q_t values reaching equilibrium by the time of the first measurement (i.e., < 10 min) for both SFGO and LFGO systems. The final q_t values were, proportionally slightly higher for the larger surface area (and greater zeta potential) SFGO system (especially noticeable at the highest dye concentration). Unfortunately, due to the time required to transfer and centrifuge the samples, it was not possible to gain measurements over a smaller time-step to completely confirm the kinetic trends. The rapid uptake of MB is consistent with previous work investigating charged dye adsorption on oppositely charged fine mineral surfaces [87], albeit with a likely faster rate achieved by the GO due to its increased specific surface area. Increasing initial dye concentration from 5 to 15 mg/l had the effect of significantly increasing the values of q_t for both GO-dye pairings, as would be expected for conditions under maximum adsorption, in which the effect of higher initial dye concentrations is to overcome the inherent resistance to mass transfer between liquid:solid phase equilibrium [88,89]. The difference between the two GO types was also more significant for the higher dye concentration. By comparison, adsorption of MO was considerably less favourable with overall q_t values less than one fifth of those for MB for both GO materials. Additionally, equilibration appears to occur after a longer time of approximately 30 min. Despite its high capacity to adsorb MB, the SFGO was not observed to have increased MO adsorption (in fact, its performance was slightly below that of the LFGO). The mechanism of dye adsorption, including analysis of the adsorption process for GO, will be discussed later (see Section 3.2.5).

Percentage dye removals were also calculated for each GO-dye pairing after 50 min contact time for initial dye loadings of 5, 10 and 15 mg/l, as shown in Fig. 4, with standard deviational error, calculated across three runs, tabulated in Table S2 within the ESM. These data again demonstrate the disparity in adsorption efficiency between cationic MB and anionic MO, but also that while the total adsorption capacity (q_t) increases with dye concentration (Fig. 3a and b), there is a slight reduction in the percentage removal as dye concentration is increased. Such differences would be expected for ion and small molecule surface adsorption, due to greater competition between adsorbate groups [90], although it is interesting that similar reductions are evident with both MB and MO despite the interaction mechanism being different.

Analysis of the various GO-dye systems by PFO and PSO modelling revealed the PSO model was better suited to predicting the kinetics (at least in terms of achieving higher R^2 values). A comparison of PFO and PSO model analysis, including all calculated and experimental parameters and linear regression coefficients, is shown in Table 2. The $q_{e,exp}$ parameter reported in the table is taken as the maximum value of q_t recorded in the experimental kinetics studies.

For the PFO model, R^2 values remained high for each GO-dye combination but were lower overall than the PSO model, indicating that the PFO model may still be appropriate in some cases. Further inspection, however, revealed there to be a significant disparity for all cases in the comparison of $q_{e,cal1}$ and experimental $q_{e,exp}$. Values in PFO cases, indicated relatively poor correlation to the longer time experimental

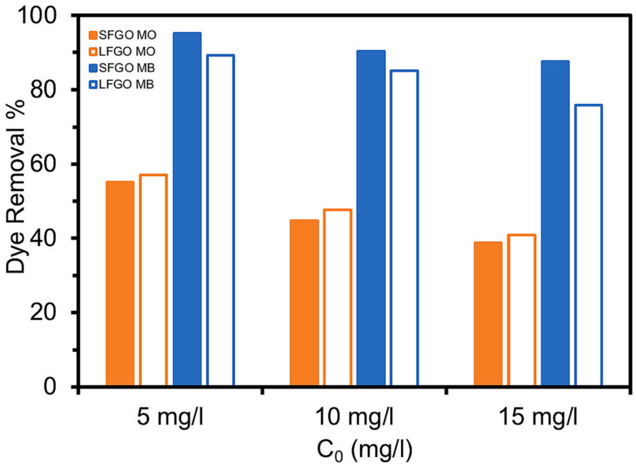

Fig. 4. Percentage dye removal as a function of initial dye concentration, for adsorption of 5, 10 and 15 mg/l MB and MO by SFGO and LFGO. The data for this figure is obtained from the previously discussed dye adsorption studies. Standard deviation in Dye Removal %, across three runs, is tabulated in Table S2 within the ESM.

data, as such, the PSO model was considered a more appropriate representation of the dye adsorption kinetics. The values of k_2, as computed from the gradients of the second order SFGO and LFGO plots, suggested that, in general, the kinetics of adsorption of MB was faster compared to the adsorption of MO, as evidenced by the larger respective PSO rate constants. Interestingly, the values of k_2 for adsorption of MB with SFGO and LFGO appeared to be slightly counter intuitive, as the values calculated for LFGO were in fact higher than the SFGO counterparts, albeit that they were the same order of magnitude and similar. This would suggest that the greater zeta potential of the SFGO is not leading to an enhanced kinetic rate of adsorption, although the final adsorbed amounts were greater (a feature consistent with the larger specific surface area). Trends in the literature regarding the impact of flake size upon adsorption efficacy have generally indicated that smaller flake size adsorbents tend to also have higher rate constants for adsorption [44,91], although, it may be other surface chemical changes are critical. Given the similar chemistry of the LFGO and SFGO, it highlights that adsorption rates are not entirely based on electrostatic attraction (as is evident from the adsorption on anionic MO systems). Additionally, as discussed, the fact that adsorption on MB occurred within the first time-step, means there is a greater degree of uncertainty on the measured k_2 values.

Table 2
PFO and PSO dye adsorption kinetics for MB and MO dyes using SFGO and LFGO.

Kinetics Model: (GO)	Initial MB Concentration (mg/l)			Initial MO Concentration (mg/l)		
	5	10	15	5	10	15
$q_{e,exp}$ (mg/g) - SFGO	96.0	182.4	265.2	27.9	45.2	58.8
$q_{e,exp}$ (mg/g) - LFGO	90.0	171.8	230	28.9	48.2	61.9
PFO: (SFGO)						
$q_{e,cal1}$ (mg/g)	50.6	82.4	102.6	20.6	45.4	55.7
k_1 (min^{-1})	0.137	0.132	0.158	0.092	0.134	0.138
R^2	0.939	0.899	0.908	0.951	0.955	0.999
PFO: (LFGO)						
$q_{e,cal1}$ (mg/g)	51.1	71.0	82.6	19.3	47.8	50.5
k_1 (min^{-1})	0.140	0.144	0.152	0.092	0.109	0.119
R^2	0.926	0.907	0.891	0.944	0.972	0.990
PSO: (SFGO)						
$q_{e,cal2}$ (mg/g)	98.0	185.2	270.3	29.9	48.3	63.3
k_2 (g/(min·mg))	0.011	0.008	0.011	0.009	0.007	0.005
R^2	0.999	0.999	1.000	0.999	1.000	0.999
PSO: (LFGO)						
$q_{e,\ cal.2}$ (mg/g)	91.7	172.4	232.6	30.5	53.2	65.8
k_2 (g/(min·mg))	0.012	0.011	0.012	0.011	0.004	0.005
R^2	1.000	1.000	1.000	0.996	0.996	0.997

3.2.2. Equilibrium of dye adsorption

Analysis of equilibrium isotherms and establishing the most appropriate equilibrium model is also an important step in explaining the behaviour of adsorbent-adsorbate systems. Equilibrium studies were carried out using higher concentrations of dye (50–150 mg/l) compared to the kinetics experiments (5–15 mg/l), and higher loadings of GO (20 mg for MB experiments and 30 mg for MO experiments) to ensure sufficient adsorbent mass:liquid ratio for the higher dye concentrations. The contact time for equilibrium studies was chosen such that the GO and dye concentrations achieved equilibration based on observations from the kinetics studies. The time chosen was 80 min, which far exceeds the amount of time required for equilibration, as established for our systems (Fig. 3).

Langmuir (homogeneous) and Freundlich (heterogeneous) adsorption isotherms were selected to analyse equilibrium data. Linearised Langmuir isotherm plots for MB and MO systems are shown in Fig. 5a and b respectively, with equilibrium lines for SFGO and LFGO included on each plot. Linearised Freundlich isotherm plots of each GO-dye system are shown in the ESM (Fig. S6). From the Langmuir analysis of equilibrium adsorption, parameters q_{max} and K_L were calculated for each GO-dye system and are presented in Table 3.

In the Freundlich isotherm, the parameter n is equal to the inverse of the isotherm gradient and is related to the intensity of adsorption. It is considered that a small value of n indicates greater intensity of adsorption, provided that the value of n exceeds unity [92]. Inspection of Table 3 reveals the values of n are lower in each GO system for MB adsorption compared to MO, highlighting that adsorption of MB by both GO systems is more intense, as may be expected. In turn, the lowest n was achieved for SFGO–MB adsorption suggesting this was the most intense and favourable adsorption process. Meanwhile, for SFGO–MO, with the highest corresponding n, was the least intense, owing in this case to the strong electrostatic repulsion. McKay et al. [93] reported that a value of n between 1 and 10 is representative of a favourable adsorption system, and as such the reported n values are all of appropriate magnitude to suggest favourability of adsorption, despite electrostatic repulsion in MO cases.

For the Langmuir isotherm, the parameter q_{max} is the maximum adsorption capacity assuming monolayer adsorption. The ordering of q_{max} values was SFGO–MB > LFGO–MB > LFGO–MO > SFGO–MO. Accordingly, the values of q_{max} reflected the expected trends based on experimental observation. The Langmuir constant, K_L, reflects the affinity of adsorption between an adsorbent and adsorbate and is correlated to the surface area and availability of surface pores [94,95]. These values suggested that the larger K_L values resulted from the adsorption of MB, thus inferring greater affinity for MB adsorption than MO.

Both Langmuir and Freundlich isotherms appear to be suitable models for our systems based on their high statistical regression coefficients. Comparison of R^2 values for Freundlich versus Langmuir models suggests the Langmuir model is more appropriate, as respective R^2 values are higher. Accordingly, the adsorption of dyes onto GO surfaces assumes a monolayer coverage, and that interaction is governed by dyes binding to a single available adsorbent site on the GO [96]. Suitability of Langmuir over Freundlich is perhaps to be expected within such a system since the Freundlich isotherm is mainly suited to experimental systems having low concentrations of contaminant (dye), provided also that the concentration range of dyes tested is limited to a strict range [97].

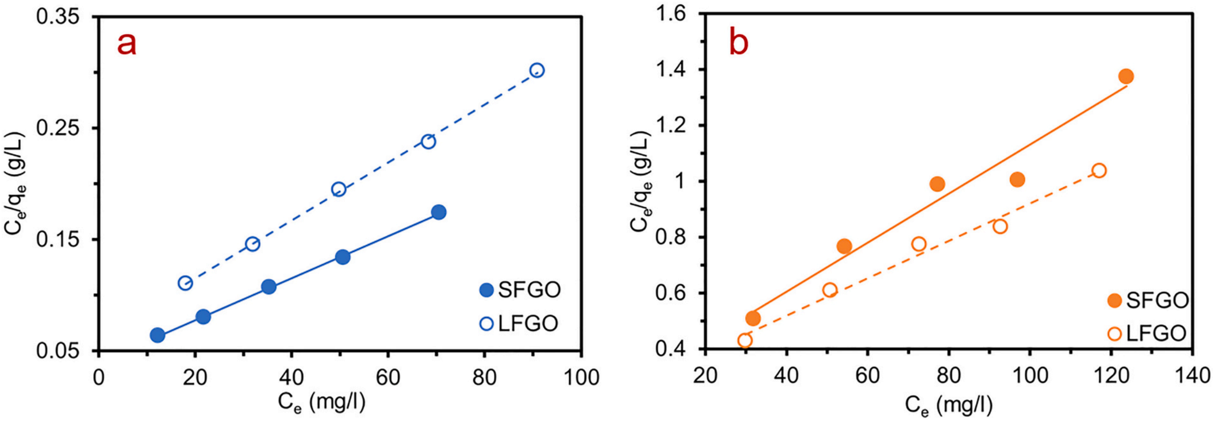

Fig. 5. Linearised Langmuir isotherm plots of a) MB adsorption and b) MO adsorption, for SFGO and LFGO systems. Initial dye concentrations were varied in the range 50–150 mg/l, while for MB experiments the GO loading was 20 mg and for MO experiments it was 30 mg.

Table 3
Langmuir and Freundlich isotherms for MB and MO adsorption by SFGO and LFGO.

	Dye	
Adsorption Isotherm: (GO)	MB	MO
Langmuir: (SFGO)		
q_{max} (mg/g)	526.3	113.6
K_L (l/g)	0.048	0.035
R^2	0.999	0.961
Langmuir: (LFGO)		
q_{max} (mg/g)	384.6	149.3
K_L (l/g)	0.041	0.027
R^2	0.999	0.984
Freundlich: (SFGO)		
K_F $((\text{mg·g})\cdot(\text{l·g}))^{1/n}$	69.2	21.2
n	2.34	3.23
R^2	0.974	0.881
Freundlich: (LFGO)		
K_F $((\text{mg·g})\cdot(\text{l·g}))^{1/n}$	55.5	19.4
n	2.60	2.67
R^2	0.976	0.978

In addition to the Langmuir and Freundlich isotherms, there are a number of alternatives in existence, including those proposed by Sips [98], Tempkin [99], Redlich–Peterson [100] and Dubinin–Radushkevich [101]. For dye adsorption studies involving GO, however, a significant number of articles have concluded that either the Langmuir [94,102–106] or Freundlich [107,108] isotherms are the most suitable, with a majority suggesting preference for the Langmuir fit (see Table 4). This may be a feature of the 2D nature of GO, which enables dye molecules to adsorb homogenously as a monolayer, despite the more complex microscopic aggregate structure of the GO. This feature would suggest that exposure to the 2D GO planes by the dye is relatively unimpeded, or a more heterogeneous adsorption may have been expected.

For each GO-dye combination, parameter R_L was plotted as a function of initial dye concentration as shown in the ESM (Fig. S7). Calculated values of R_L all lie in the range 0–1, indicating that the process of adsorption was favourable for each GO–dye system across the range of initial dye concentrations [96,109,110]. In all cases, the R_L values tend towards zero as dye concentration increased in the range 50–150 mg/l (given that R_L α $1/C_{0}$, as per Eq. (8)), implying that an increase in dye concentration was correlated to an increase in favourability of adsorbate–adsorbent interaction [111,112].

Table 4
Literature sample of carbon-based adsorbents used in adsorption studies of MB and MO dyes.

Adsorbent [Ref.]	Dye	Equilibrium isotherm	q_{max} (mg/g)	Kinetics Model	$q_{e,cal.}$ (mg/g)
SFGO (This Study)	MB, MO	Langmuir	526.3, 113.6	PSO	270.27, 63.29
LFGO (This Study)	MB, MO	Langmuir	386.4, 149.3	PSO	232.56, 65.79
Reduced GO [38]	MB	Langmuir	121.95	PSO	70.72
Graphene nanoplatelets [113]	MB	Langmuir	245.5	PFO	140.95
GO [37]	MB	Langmuir	598	PFO	599.8
GO [102]	MB	Langmuir	243.9	PFO	243.9
GO [114]	MO	Langmuir	16.83	PSO	0.096
GO [103]	MB	Langmuir	1939	–	–
Activated Carbon [115]	MO	Freundlich	336.12	PSO	200.34

Carbon-based adsorbents are increasingly utilised in the adsorption of dyes, amongst a host of other species including heavy metal ions. Table 4 provides a literature sample of the performance of several carbon-based adsorbents, in particular GO materials, in terms of their MB and/or MO adsorption. The results obtained in our study are likewise provided in the table. From the table, it is facile to observe the preference for the Langmuir isotherm and PSO kinetics model. It appears that the results obtained in our studies regarding the adsorption of MB and MO are consistent with examples from the literature and that the model parameters obtained by our analysis suggest that our GO particular materials are able to sorb dyes with high efficacy, in comparison with competitors.

The issue of reusability of GO-based adsorbents has featured in a number of dye adsorption studies [116–118]. The ability to regenerate adsorbent species downstream may offer advantages in terms of cost-effectiveness and ultimately, reduction in energy and water consumption during the processing of the adsorbent. Although we do not report on the reusability of our commercial GO systems in dye adsorption, it is acknowledged that this is also a salient step in the developmental timeline of commercial GOs, and a number of existing studies have been provided here to highlight progress in adsorbent recycling techniques. Existing regeneration methods have predominantly focussed on chemical techniques, in which the adsorbed dye molecules are stripped from GO using acid [119] or alkali [120], with the adsorbent subsequently washed in water. In one study [121], GO was recycled over five adsorption cycles with less than 10% drop in adsorption capacity compared to the first cycle. An alternative promising technique involves separation of GO from dye by application of microwave heating [122], which is attractive due to the limited space required for its implementation.

3.2.3. Aggregation of GO in dye

In Section 3.2.1, the aggregation of GO in dye was briefly described by inspection of the images regarding the effect of contact time on kinetics of adsorption (Fig. 3c and 3d). Aggregation of GO in dye is typically an undesirable phenomenon in an adsorption process, as effective adsorption is reliant upon the existence of GO sheets in exfoliated, homogeneous state, thus promoting the adsorption of dye onto binding sites by maximising the contact area availability of GO [123,124]. However, such aggregation post-adsorption, may lead to easier separation in downstream processes, thus offering potential for development of selective adsorption systems, in which individual dyes may be regenerated from a mixture [125]. GO flakes were demonstrated by measurement of zeta potential (Fig. 1d) to possess highly negative surface charges across pH 3.5–10.0, enabling them to resist aggregation. However, contacting the GO with a charged species, such as salt or dye, which is capable of screening the electronegativity of the GO has been demonstrated to overcome this resistance resulting in aggregation [31,126,127]. In Fig. S8, images of GO-dye dispersions are provided, showing GO dispersed in (a) MB and (b) MO. While in the case of MO, aggregation of GO was not observable by the naked eye, for MB large particulates were clearly generated which then sedimented to the base of the sample vials over extended contact times. It appears for MB in particular, neutralisation of the electrostatic charge of the GO resulted in high levels of flake aggregation. Such physical changes may limit the recyclability of GO to remove these types of dyes, in which the charge of the dye is having a discernible impact on the stability of the GO [128].

In order to investigate the aggregation of GO in our selected dyes, laser diffraction (LD) was utilised to measure changes in particle size distribution. Fig. 6a and b show the PSDs for SFGO and LFGO, respectively, dispersed in 15 mg/l MB and MO. The PSDs obtained for SFGO and LFGO in distilled water (i.e., as presented in Fig. S2 in the ESM) are also shown on these plots to allow comparison. The corresponding d (10), d(50) and d(90) values obtained in LD analysis of the aggregates are provided in Table S3.

Measurement of zeta potential was used to confirm the electrokinetic changes to the GO surface charge upon dye adsorption. Fig. 6c and d show the zeta potential of SFGO and LFGO dispersed in 5, 10 and 15 mg/l of (c) MB and (d) MO solutions. For reference, the corresponding potential of the GO in distilled water is provided in each plot, at respective dye concentrations of zero.

Inspection of the PSDs and associated parameters in Table S3 of the ESM for SFGO and LFGO reveals that SFGO (Fig. 6a) and LFGO (Fig. 6b) tend to aggregate with both MB and MO dyes, albeit to much larger degrees with the MB. Consistent with the nominal flake sizes, the LFGO aggregates are also larger than the SFGO with both dyes.

Measurement of zeta potential confirmed that the interaction of GO with dye had a marked effect upon the electrokinetic properties of the GO. Neutralisation and reversal of the negative GO surface charge by MB was evident across the range of MB concentrations (Fig. 6c), with the zeta potential actually becoming slightly positive, in both cases. As such, neutralisation of charge has been demonstrated to be a salient feature relating to the aggregation of GO flakes in cationic dyes. Aggregation could lead, therefore, both through the lack of electrostatic stability and secondary attractive interactions between the adsorbed MB dye itself. It appears the overall interactions for the LFGO and SFGO are similar, with

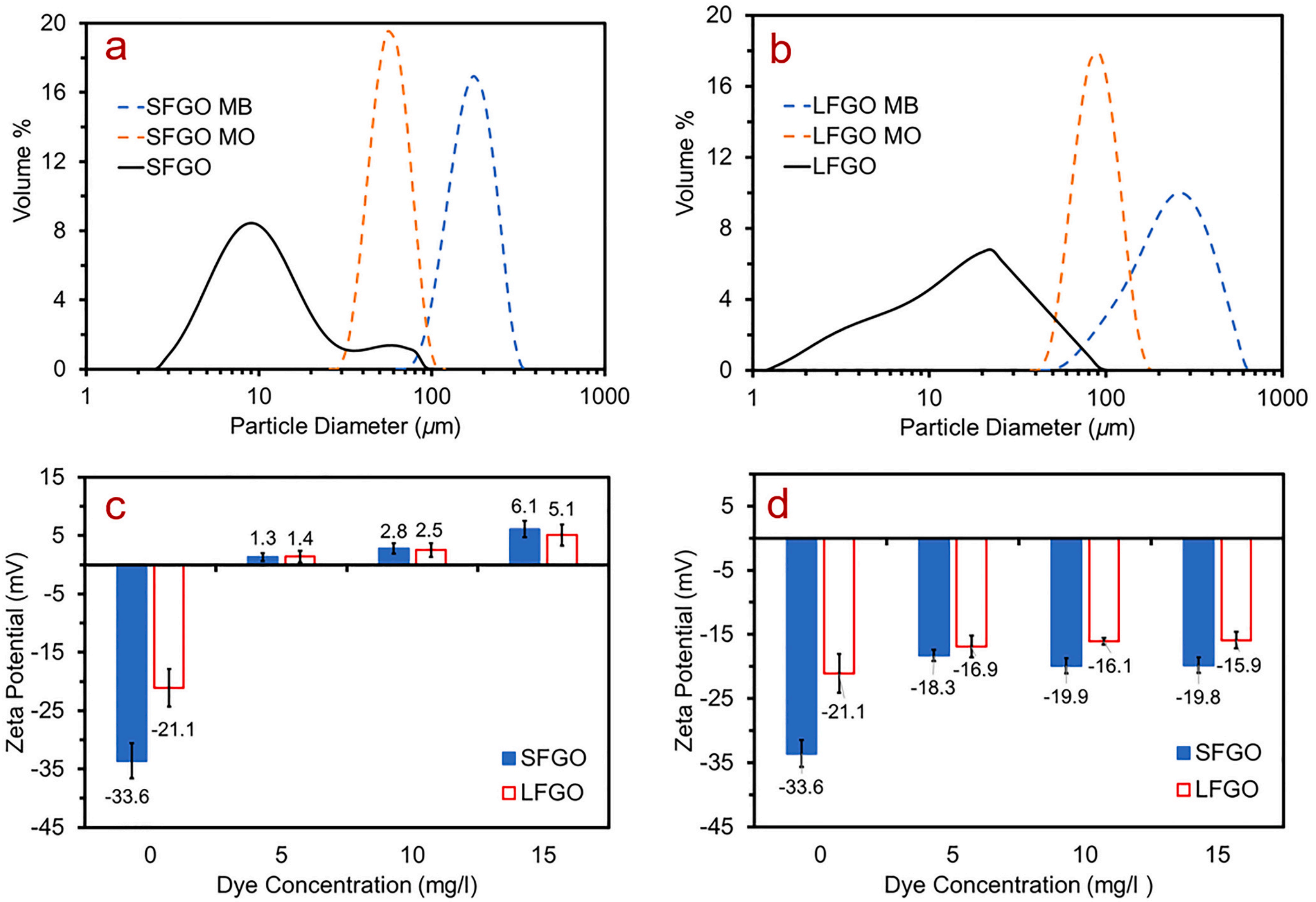

Fig. 6. Sizing of (a) SFGO and (b) LFGO aggregates in MB and MO using LD technique and Zeta Potential of (c) GO-MB and (d) GO-MO aggregates. Vertical error bars in (c) and (d) represent standard deviation across three separate runs.

the larger aggregates in the case of LFGO likely being resultant from the larger sized (yet lower surface area) individual starting units.

Aggregation of GO in anionic dyes is not as well described in the literature. In the case of GO dispersion in MO solutions (Fig. 6d) charge neutralisation did not occur, as expected, and electronegativity was maintained across the concentration range of dyes. Interestingly, the zeta potential did reduce in magnitude as a result of dispersing GO in MO, which is likely an effect of double layer suppression from the effective electrolyte addition in the dye solution [107]. However, this suppression is relatively small in magnitude, and not the dominant factor in aggregation, which is more likely driven through attractive groups on the adsorbed MO. For example, hydrogen bonding or *π*–*π* stacking between aromatic groups on adsorbent and adsorbate molecules can lead to strong association [129].

3.2.4. The impact of salt addition on adsorption of MB

Thus far, we have considered dye removal from water by adsorption of dye molecules onto GO adsorbent surfaces in a somewhat idealised system consisting of dye and adsorbent only. Here, we have extended our study to consider the effect of adding sodium sulphate and magnesium sulphate to MB solutions. MB was selected as the dye of choice, owing to its electrostatic attraction to GO. The simulated "dye-salt" solution may be considered a step closer to a real textile effluent, which in practice comprises a complex mixture of components. We have seen that both SFGO and LFGO have a high proclivity for adsorption of MB, which is reflected in the high adsorption capacities of both materials. Adding charged electrolytes to the dye mix enables us to explore the impact of foreign ions on dye adsorption capacity.

Values of q_t as a function of time for adsorption of a 15 mg/l loading of MB by SFGO and LFGO with dispersed sodium sulphate or magnesium sulphate salt are shown in Fig. 7a and b, with associated standard deviational error in q_t for salt concentrations 0.50–2.00 g/l across three runs provided in Table S4, in the ESM. The error for the case of "No Salt" may be obtained from the relevant SFGO or LFGO line of the 15 mg/l dye concentration, in Table S1 of the ESM. For brevity, sodium sulphate is indicated in the plots by Na^+, and magnesium sulphate as Mg^{2+}. We observed that increasing salt concentration from 0 to 2.0 g/l had the effect of markedly reducing the overall q_t in comparison to the cases in which there was no electrolyte present. This effect was much more pronounced for both GOs in the presence of the divalent Mg^{2+} versus monovalent Na^+.

The linear PSO kinetic model was fitted to the experimental data in an analogous fashion to the case in which no salt was added, and values of $q_{e,cal2}$ were extracted from the plots. The variation in calculated $q_{e,cal2}$ versus salt concentration, with fitted linear trend line and corresponding statistical R^2, are shown in Fig. 8a. It is apparent that adding Mg^{2+} ions caused a more significant reduction in $q_{e,cal2}$ as electrolyte concentration increased.

For SFGO, $q_{e,cal2}$ decreased from 270.27 mg/g when no salt was added to 256.41 mg/g (5.13% reduction) for Na^+ addition, and to 204.08 mg/g (32.43% reduction) for Mg^{2+} addition when the salt concentration was 2.0 g/l. Similarly, for the LFGO the effect on $q_{e,cal.2}$ decreased from 232.56 mg/g when no salt was added to 217.39 mg/g (6.98% reduction) for 2.0 g/l Na^+ addition, and 192.31 mg/g (17.31% reduction) for 2.0 g/l Mg^{2+} addition (importantly noting the effective reduction with Mg^{2+} with LFGO was around half that of the SFGO reduction).

One important consideration was to understand why the influence of Mg^{2+} was more significant for the SFGO than the LFGO system. To investigate the role of salt addition upon electrokinetic stability, the zeta potential of the GO-in-water colloid was measured across a range of salt concentrations, in a similar fashion to Baskoro et al. [72], as shown in Fig. 8b. It is apparent that the addition of Mg^{2+} had a much greater charge screening effect upon the negatively charged GO sheets compared to the addition of Na^+. In fact, at sufficient ionic concentration, addition of Mg^{2+} resulted in charge reversal as indicated by the shift to positivity of the potential, as adsorbed Mg^{2+} ions fully occupied the binding sites on the GO surface and excess cations remaining in solution resulted in the positive charge [31]. For SFGO, it appeared that the point of charge reversal is lower (i.e., requiring the addition of less Mg^{2+}), compared to LFGO, probably as the initial electrostatic attraction is larger. This feature correlates to the more severe decline in values of $q_{e,cal2}$ for the SFGO systems with Mg^{2+} addition, as evident in Fig. 8a. Further discussion regarding the mechanism of dye adsorption subject to the presence of electrolytes is provided in the mechanistic discussion section (Section 3.2.5).

3.2.5. Discussion: mechanism of dye adsorption

In this paper, we have reported on the kinetics and equilibria of dye adsorption onto GO adsorbent surfaces. Experimental data has been analysed using widely utilised PFO and PSO kinetics models and Langmuir and Freundlich adsorption isotherms. Adsorption of dyes onto both SFGO and LFGO was governed according to a PSO kinetics model and the Langmuir adsorption isotherm.

Electrostatic interactions are considered to be a significant factor in the adsorption mechanism of cationic MB. Measurement of zeta potential for both SFGO and LFGO (Fig. 1d) revealed that both materials possess significant negative potentials, and that across the pH range the

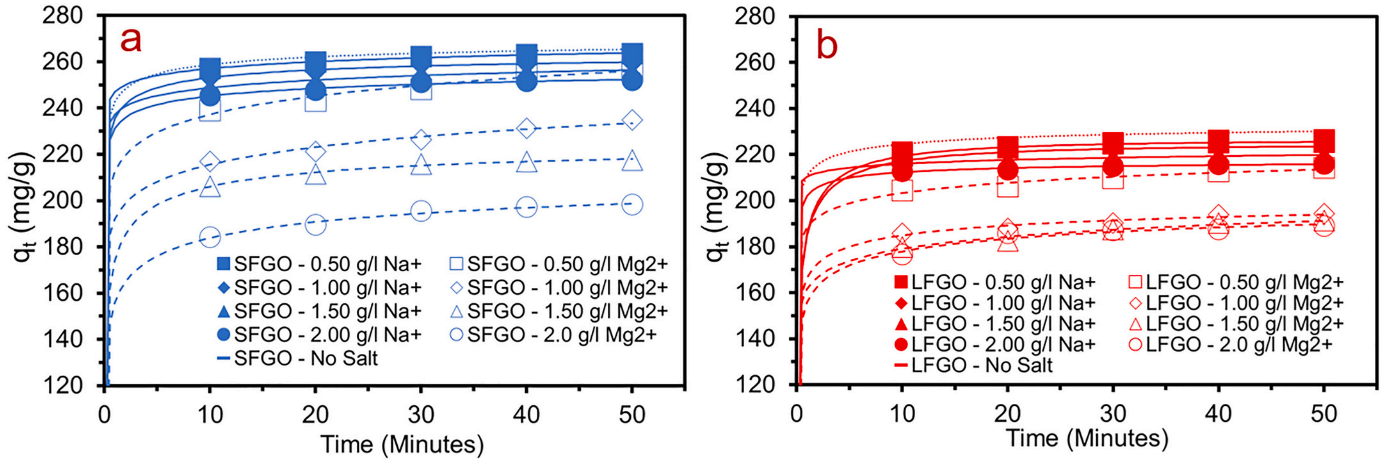

Fig. 7. Calculated values of q_t as a function of time for 15 mg/l initial dye concentrations in a) MB-SFGO and b) MB-LFGO systems. For these experiments, salt concentration was varied between 0 and 2.0 g/l, using 5 mg GO and the values of q_t generated as before. Standard deviational errors in q_t values is provided in Table S4 of the ESM.

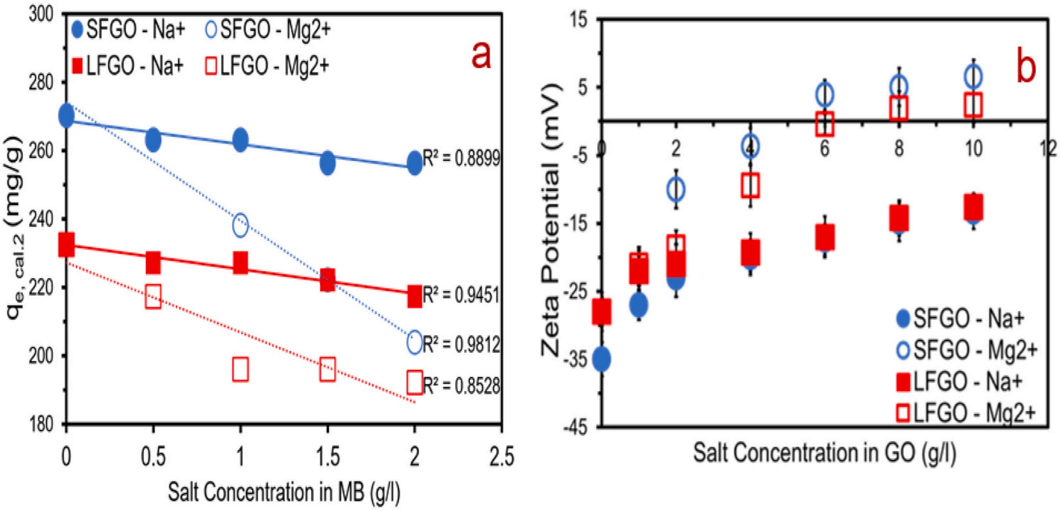

Fig. 8. a) Calculated values of $q_{e,\ cal.2}$ from the PSO kinetics model for adsorption of MB by SFGO and LFGO in MB-Na_2SO_4 and MB-$MgSO_4$ systems, and b) Zeta potential of GO-salt colloids, for salt concentrations ranging from 0 to 10 g/l in 0.01 mg/ml GO.

magnitude was greater for SFGO than LFGO. Peng et al. [130] explained this has the bifold effect of enhancing the dispersion of GO in water, but also promoting the electrostatic attraction between negatively charged GO and positively charged MB. The mechanism of interaction is governed by strong electrostatic interaction between GO and MB, meanwhile, π–π interactions between the cationic dye and the conjugated π system in the GO are also a feature [25]. Sharma and Das [35] postulated that cationic methyl green is attracted in particular to deprotonated –COOH groups present on the GO, suggesting that adsorption of cationic dyes takes place at the edges of the GO sheets.

In our studies, both GOs were found to be poorer adsorbents of anionic MO compared to cationic MB, as reflected by both kinetics and equilibria findings, although significant adsorption was still evident, despite the electrostatic repulsion. MO is also able to interact with adsorbents via π–π interactions and hydrogen bonding, accounting for the adsorption we did observe [25,131]. In the case of GO–MO systems, however, electrostatic repulsion is clearly a dominating feature, as repulsion significantly inhibits these interactions from taking place [132]. Kinetics and equilibrium studies for MO adsorption demonstrated that, unlike with the MB, the higher specific surface area of the SFGO did not lead to any increase in adsorption (and in fact, adsorption was weaker with the SFGO). This is again, likely mostly due to the electrostatic interactions, as the SFGO had greater charge, making it more electrostatically repulsive. Chemical analyses did not indicate considerable differences in surface chemistry of the two GOs, with exception that XPS demonstrated a slightly higher oxygen content in the LFGO sample.

The effects of electrolyte ions on the adsorption of MB by SFGO and LFGO was also investigated. In the binary GO adsorbent–MB system, adsorption of MB by GO was unhindered since it wasn't impeded by the presence of other charged species. Dissolution of electrolyte ions into the dye resulted in Na^+ and Mg^{2+} cations altering the electrostatic double layer, and competing with MB for adsorbent occupancy sites on the GO surface and, as a result, the PSO dye adsorption capacities ($q_{e,cal2}$ values) declined (Fig. 8a). This effect was particularly stark for divalent Mg^{2+} addition, where due to its multivalency, it facilitates adsorption onto GO directly (while the effects of Na^+ are thought to be mostly from associated changes to the double layer) [31,72,133]. The binding of Mg^{2+} is postulated to be particularly strong for bidentate ligands on GO, such as deprotonated –COOH. The effect of adding Mg^{2+} to GO was highlighted by consideration of the zeta potential, in which it was observed that sufficient concentration of Mg^{2+} causes complete charge neutralisation of the GO sheets. This resulted in a significant reduction in values of $q_{e,cal2}$, owing to the occupancy of binding sites by metal cations. In the case of Na^+ addition, the impact upon $q_{e,cal.2}$ values were evidently more minimal; it is proposed that this is due to the limited adsorption of Na^+ cations onto GO. Na^+ cations were also revealed to have a small impact upon the zeta potential of the GO, although high ionic concentrations did lower the magnitude. As the Na^+ cations are electrically attracted to negative GO, they can accumulate in the electrical double layer of the GO sheets as counterions, causing compression of the double layer and impacting the measured zeta potential (although the true surface potential is not altered) [134,135].

4. Conclusions

In this study, two commercially available GO materials, of different flake sizes, have been characterised and tested for their adsorption performance of anionic MO and cationic MB dyes. Dye adsorption studies, including kinetics and equilibrium modelling, demonstrated that the GOs were excellent adsorbents of cationic MB, whereas they were less effective for anionic MO. Furthermore, the introduction of cations into MB solutions, in the form of sodium and magnesium sulphate salts, was demonstrated to have the effect of reducing dye adsorption capacity, particularly in the case of the latter. Critically, complete charge reversal was observed with Mg^{2+} solutions, due to the direct electrostatic adsorption of these divalent cations. Monovalent Na^+ cations are incapable of such adsorption, as such, their impact upon MB adsorption was significantly lower, overall. The main mechanism for dye adsorption with MB was attributed to electrostatic attraction between GO and the dye. The smaller flake size SFGO was considered important in promoting adsorption of MB, due to higher specific surface area and associated availability of adsorption sites, while it also had a greater magnitude of zeta potential. Interestingly, while adsorption with anionic MO was reduced, it was still considerable at >100 mg/g for both flake sizes.

This research has provided a detailed investigation into the potential application of commercially available GOs as a material adsorbent in industrial wastewater treatment, presenting insights which may assist practitioners in specifying or selecting materials. It is hoped that our studies will provide understanding into the benefits of commercial GO technologies, and act as a stepping stone from which existing GO materials may be developed for the provision of scalable technology, which is economically and contextually attractive for industrial use.

CRediT authorship contribution statement

James M. Exley: Conceptualization, Methodology, Formal analysis, Validation, Investigation, Data curation, Writing – original draft. **Timothy N. Hunter:** Supervision, Conceptualization, Methodology, Writing – review & editing. **Thomas Pugh:** Supervision, Conceptualization, Methodology, Writing – review & editing. **Martin R. Tillotson:** Project administration, Supervision, Conceptualization, Methodology, Writing – review & editing.

Declaration of Competing Interest

The authors declare the following financial interests/personal relationships which may be considered as potential competing interests:

Martin Tillotson reports financial support was provided by UK Research and Innovation.

Data availability

Data will be made available on request.

Acknowledgements

This study was supported by funding through a University of Leeds doctoral award from Engineering and Physical Sciences Research Council (EPSRC) UK and Evove Limited (grant references EP/M50807X/1, EP/R513258/1). The authors are grateful to the funders and acknowledge their support of this work.

The authors would like to express gratitude to the following, based in University of Leeds, who have provided technical support and/or training: Dr. Ben Douglas (BET, laser diffraction, dynamic light scattering, zeta potential), Ms. Lucy Leonard (FTIR), Dr. Faye Esat (XRD), Dr. Andrew Britton (XPS), Dr. Alexander Kulak (Raman Spectroscopy). The Henry Royce Institute have funded the XPS equipment and thus made the analysis possible. In addition, Ms. Karen Stevens, Dr. David Elliott, Mr. Morgan McGowan and Ms. Emma Tidswell have provided technical support and training in relation to dye adsorption studies, including safe setup and operation of the equipment.

Appendix A. Supplementary data

Supplementary data to this article can be found online at https://doi.org/10.1016/j.powtec.2023.118387.

References

[1] J.M. Aquino, R.C. Rocha-Filho, L. Ruotolo, N. Bocchi, S.R. Biaggio, Electrochemical degradation of a real textile wastewater using beta-PbO2 and DSA (R) anodes, Chem. Eng. J. 251 (2014) 138–145.
[2] M.M. Hassan, Christopher M. Carr, A critical review on recent advancements of the removal of reactive dyes from dyehouse effluent by ion-exchange adsorbents, Chemosphere 209 (2018) 201–219.
[3] S. Sarkar, et al., Decolourisation and biodegradation of textile Di-azo Dye Congo Red by Chryseobacterium geocarposphaerae DD3, Sustainability 13 (19) (2021).
[4] M. Ismail, et al., Pollution, Toxicity and Carcinogenicity of Organic Dyes and their Catalytic Bio-Remediation, 2019.
[5] R. Ganesh, G.D. Boardman, D. Michelsen, Fate of azo dyes in sludges, Water Res. 28 (6) (1994) 1367–1376.
[6] V. Jegatheesan, et al., Treatment of textile wastewater with membrane bioreactor: a critical review, Bioresour. Technol. 204 (2016) 202–212.
[7] H.S. Erkan, et al., Performance evaluation of conventional membrane bioreactor and moving bed membrane bioreactor for synthetic textile wastewater treatment, J. Water Process Eng. 38 (2020) 101631.
[8] D.A. Yaseen, M. Scholz, Textile dye wastewater characteristics and constituents of synthetic effluents: a critical review, Int. J. Environ. Sci. Technol. 16 (2019) 1193–1226.
[9] M.N. Rashed, in: M.N. Rashed (Ed.), Adsorption Technique for the Removal of Organic Pollutants from Water and Wastewater, in Organic Pollutants - Monitoring, Risk and Treatment, Intech Publisher Croatia: Croatia, Croatia, 2013.
[10] S.R.C.K. Rajendran, B. Mason, A.A. Doucette, Review of membrane separation models and technologies: processing complex food-based biomolecular fractions, Food Bioprocess Technol. 14 (3) (2021) 415–428.
[11] A. Prasetyaningrum, et al., Photochemical oxidation process of copper from electroplating wastewater: process performance and kinetic study, Processes 8 (10) (2020).
[12] S.K. Loeb, et al., The technology horizon for photocatalytic water treatment: sunrise or sunset? Environ. Sci. Technol. 53 (6) (2019) 2937–2947.
[13] M.A. Almaradhi, H.M. Hassan, M.S. Alhumaimess, Fe3O4-carbon spheres core–shell supported palladium nanoparticles: a robust and recyclable catalyst for suzuki coupling reaction, Chin. J. Chem. Eng. 51 (2022) 75–85.
[14] H. Xue, et al., Efficient adsorption of anionic azo dyes on porous heterostructured MXene/biomass activated carbon composites: experiments, characterization, and theoretical analysis via advanced statistical physics models, Chem. Eng. J. 451 (2023) 138735.
[15] M.M. Sabzehmeidani, et al., Carbon based materials: a review of adsorbents for inorganic and organic compounds, Mater. Adv. 2 (2) (2021) 598–627.
[16] Á. Santana-Mayor, et al., 4 - Carbon-based adsorbents, in: C.F. Poole (Ed.), Solid-Phase Extraction, Elsevier, 2020, pp. 83–127.
[17] W. Peng, H. Li, Y. Liu, S. Song, A review on heavy metal ions adsorption from water by graphene oxide and its composites, J. Mol. Liq. 230 (2017) 496–504.
[18] S. Tamjidi, H. Esmaeili, B.K. Moghadas, Adsorption of heavy metal ions by various low-cost adsorbents: a review, Mater. Res. Express (2019) 6.
[19] G.K. Ramesha, et al., Graphene and graphene oxide as effective adsorbents toward anionic and cationic dyes, J. Colloid Interface Sci. 361 (1) (2011) 270–277.
[20] J.W. Suk, et al., Mechanical properties of monolayer graphene oxide, ACS Nano 4 (11) (2010) 6557–6564.
[21] X. Mu, et al., Thermal transport in graphene oxide – from ballistic extreme to amorphous limit, Sci. Rep. 4 (1) (2014) 3909.
[22] M. Panahi-Sarmad, et al., Tuning the surface chemistry of graphene oxide for enhanced dielectric and actuated performance of silicone rubber composites, ACS Appl. Electron. Mater. 1 (2) (2019) 198–209.
[23] M.S. Soltan, et al., Copper nanoparticle-decorated RGO electrodes as hole transport layer of perovskite solar cells enhancing efficiency and shelf stability, J. Mater. Res. Technol. 14 (2021) 631–638.
[24] H.M. Hassan, et al., Sulfanilic acid-functionalized magnetic GO as a robust adsorbent for the efficient adsorption of methylene blue from aqueous solution, J. Mol. Liq. 361 (2022) 119603.
[25] J. Xiao, et al., Environmentally friendly reduced graphene oxide as a broad-spectrum adsorbent for anionic and cationic dyes via π–π interactions, J. Mater. Chem. A 4 (31) (2016) 12126–12135.
[26] C.R. Minitha, et al., Adsorption behaviour of reduced graphene oxide towards cationic and anionic dyes: co-action of electrostatic and π – π interactions, Mater. Chem. Phys. 194 (2017) 243–252.
[27] D. Chen, H. Feng, J. Li, Graphene oxide: preparation, functionalization, and electrochemical applications, Chem. Rev. 112 (11) (2012) 6027–6053.
[28] F. Perreault, et al., Biofouling mitigation in forward osmosis using graphene oxide functionalized thin-film composite membranes, Environ. Sci. Technol. 50 (11) (2016) 5840–5848.
[29] D. Li, et al., Processable aqueous dispersions of graphene nanosheets, Nat. Nanotechnol. 3 (2) (2008) 101–105.
[30] Y. Lu, et al., Theoretical insights into origin of graphene oxide acidity and relating behavior of oxygen-containing groups in water, Carbon 183 (2021) 355–361.
[31] M. Wang, et al., The dispersion and aggregation of graphene oxide in aqueous media, Nanoscale 8 (30) (2016) 14587–14592.
[32] T. Szabo, P. Maroni, I. Szilagyi, Size-dependent aggregation of graphene oxide, Carbon 160 (2020) 145–155.
[33] N.H. Othman, et al., Adsorption kinetics of methylene blue dyes onto magnetic graphene oxide, J. Environ. Chem. Eng. 6 (2) (2018) 2803–2811.
[34] Y. Sun, et al., Lightweight graphene oxide-based sponges with high compressibility and durability for dye adsorption, Carbon 160 (2020) 54–63.
[35] P. Sharma, M.R. Das, Removal of a cationic dye from aqueous solution using graphene oxide nanosheets: investigation of adsorption parameters, J. Chem. Eng. Data 58 (1) (2013) 151–158.
[36] W.S. Hummers, R.E. Offeman, Preparation of graphitic oxide, J. Am. Chem. Soc. 80 (6) (1958) 1339.
[37] H. Yan, et al., Effects of the oxidation degree of graphene oxide on the adsorption of methylene blue, J. Hazard. Mater. 268 (2014) 191–198.
[38] F. Arias Arias, et al., The adsorption of methylene blue on eco-friendly reduced graphene oxide, Nanomaterials (Basel, Switzerland) 10 (4) (2020) 681.
[39] X. Zhang, C. Qin, S. Jia, Co-adsorption of an anionic dye in the presence of a cationic dye and a heavy metal ion by graphene oxide and photoreduced graphene oxide, RSC Adv. 9 (2019) 5313–5324.
[40] J. Castle, A. Salvi, Interpretation of the Shirley background in x-ray photoelectron spectroscopy analysis, J. Vac. Sci. Technol. A 19 (4) (2001) 1170–1175.
[41] M. Seah, M. Brown, Validation and accuracy of software for peak synthesis in XPS, J. Electron Spectrosc. Relat. Phenom. 95 (1) (1998) 71–93.
[42] Y.-S. Ho, G. McKay, Pseudo-second order model for sorption processes, Process Biochem. 34 (5) (1999) 451–465.
[43] R. Ezzati, Derivation of pseudo-first-order, pseudo-second-order and modified pseudo-first-order rate equations from Langmuir and Freundlich isotherms for adsorption, Chem. Eng. J. 392 (2020) 123705.
[44] A.M. Aljeboree, A.N. Alshirifi, A.F. Alkaim, Kinetics and equilibrium study for the adsorption of textile dyes on coconut shell activated carbon, Arab. J. Chem. 10 (2017) S3381–S3393.
[45] B. Subramanyam, A. Das, Linearised and non-linearised isotherm models optimization analysis by error functions and statistical means, J. Environ. Health Sci. Eng. 12 (1) (2014) 1–6.

[46] M.F. Elkady, H. Shokry Hassan, E.M. El-Sayed, Basic violet decolourization using alginate immobilized nanozirconium tungestovanadate matrix as cation exchanger, J. Chem. (2015) 385741.

[47] C.H. Bolster, G.M. Hornberger, On the use of linearized Langmuir equations, Soil Sci. Soc. Am. J. 71 (6) (2007) 1796–1806.

[48] J. Zhou, et al., Preparation of graphene oxide composites and assessment of their adsorption properties for lanthanum (III) 11 (9) (2021) 1040.

[49] S.W. Andrews, D.M. Nover, J.E. Reuter, S.G. Schadlow, Limitations of laser diffraction for measuring fine particles in oligotrophic systems: pitfalls and potential solutions, Water Resour. Res. 47 (2011).

[50] J. Grubbs, et al., Comparison of laser diffraction and image analysis techniques for particle size-shape characterization in additive manufacturing applications, Powder Technol. 391 (2021) 20–33.

[51] K. Kavyashree, et al., Effect of graphite particle size on oxidation of graphene oxide prepared by modified Hummers method 2265 (1) (2020) 030096.

[52] S.Y. Chee, et al., Influence of parent graphite particle size on the electrochemistry of thermally reduced graphene oxide, Phys. Chem. Chem. Phys. 14 (37) (2012) 12794–12799.

[53] M. Mahmoudian, Mahmoud Ghasemi Kochameshki, The performance of polyethersulfone nanocomposite membrane in the removal of industrial dyes, Polymer (2021) 224.

[54] Y. Li, J. Ding, J. Chen, C. Xu, B. Wei, J. Liang, D. Wu, Preparation of ceria nanoparticles supported on carbon nanotubes, Mater. Res. Bull. 37 (2) (2002) 313–318.

[55] A.N.A. El-Hendawy, Influence of HNO3 oxidation on the structure and adsorptive properties of corncob-based activated carbon, Carbon 41 (4) (2003) 713–722.

[56] W.H. Bragg, The reflection of X-rays by crystals, Nature 91 (2280) (1913) 477.

[57] W. Liu, G. Speranza, Tuning the oxygen content of reduced graphene oxide and effects on its properties, ACS Omega 6 (9) (2021) 6195–6205.

[58] K. Krishnamoorthy, M. Veerapandian, K. Yun, S.-J. Kim, The chemical and structural analysis of graphene oxide with different degrees of oxidation, Carbon 53 (2013) 38–49.

[59] J.L.S. Gascho, et al., Graphene oxide films obtained by vacuum filtration: X-ray diffraction evidence of crystalline reorganization, J. Nanomater. 2019 (2019) 5963148.

[60] L. Stobinski, et al., Graphene oxide and reduced graphene oxide studied by the XRD, TEM and electron spectroscopy methods, J. Electron Spectrosc. Relat. Phenom. 195 (2014) 145–154.

[61] R. Siburian, et al., Performance of graphite and graphene as electrodes in primary cell battery, J. Phys. Conf. Ser. 1116 (2018) 042034.

[62] X. Jiao, et al., Comparison of the characteristic properties of reduced graphene oxides synthesized from natural graphites with different graphitization degrees, RSC Adv. 7 (82) (2017) 52337–52344.

[63] J.-B. Wu, et al., Raman spectroscopy of graphene-based materials and its applications in related devices, Chem. Soc. Rev. 47 (5) (2018) 1822–1873.

[64] A. Kaniyoor, Ramaprabhu Sundara, A Raman spectroscopic investigation of graphite oxide derived graphene, AIP Adv. 2 (3) (2012).

[65] C. Lee, et al., Measurement of the elastic properties and intrinsic strength of monolayer graphene, Science 321 (5887) (2008) 385–388.

[66] S.-G. Kim, et al., Layer-by-layer assembled graphene oxide films and barrier properties of thermally reduced graphene oxide membranes 14, 2013, pp. 247–250.

[67] H. Ribeiro, et al., Multifunctional nanocomposites based on tetraethylenepentamine-modified graphene oxide/epoxy, Polym. Test. 43 (2015) 182–192.

[68] G.P. Kotchey, et al., The enzymatic oxidation of graphene oxide, ACS Nano 5 (3) (2011) 2098–2108.

[69] A.C. Ferrari, J. Robertson, Interpretation of Raman spectra of disordered and amorphous carbon, Phys. Rev. B 61 (20) (2000) 14095–14107.

[70] J. Yin, G. Zhu, B. Deng, Graphene oxide (GO) enhanced polyamide (PA) thin-film nanocomposite (TFN) membrane for water purification, Desalination 379 (2016) 93–101.

[71] G. Midekessa, et al., Zeta potential of extracellular vesicles: toward understanding the attributes that determine colloidal stability, ACS Omega 5 (27) (2020) 16701–16710.

[72] F. Baskoro, et al., Graphene oxide-cation interaction: inter-layer spacing and zeta potential changes in response to various salt solutions, J. Membr. Sci. 554 (2018) 253–263.

[73] B. Konkena, S. Vasudevan, Understanding aqueous dispersibility of graphene oxide and reduced graphene oxide through pKa measurements, J. Phys. Chem. Lett. 3 (7) (2012) 867–872.

[74] F.A. Stevie, C.L. Donley, Introduction to x-ray photoelectron spectroscopy, J. Vac. Sci. Technol. A 38 (6) (2020) 063204.

[75] H.-H. Huang, et al., Structural evolution of hydrothermally derived reduced graphene oxide, Sci. Rep. 8 (1) (2018) 6849.

[76] F.T. Johra, J.-W. Lee, W.-G. Jung, Facile and safe graphene preparation on solution based platform, J. Ind. Eng. Chem. 20 (5) (2014) 2883–2887.

[77] R. Al-Gaashani, et al., XPS and structural studies of high quality graphene oxide and reduced graphene oxide prepared by different chemical oxidation methods, Ceram. Int. 45 (11) (2019) 14439–14448.

[78] H. Chang, et al., Regulating infrared Photoresponses in reduced graphene oxide phototransistors by defect and atomic structure control, ACS Nano 7 (7) (2013) 6310–6320.

[79] R. Muzyka, et al., Oxidation of graphite by different modified Hummers methods, New Carbon Mater. 32 (1) (2017) 15–20.

[80] L. Torrisi, et al., Graphene oxide as a radiation sensitive material for XPS dosimetry, Vacuum 173 (2020) 109175.

[81] S. Drewniak, et al., Studies of reduced graphene oxide and graphite oxide in the aspect of their possible application in gas sensors, Sensors 16 (1) (2016) 103.

[82] L.A. Shahriary, Anjali Athawale, Graphene oxide synthesized by using modified Hummers approach, Int. J. Renew. Energy Environ. Eng. 2 (2014) 58–63.

[83] L. Dhar, et al., Adsorption mechanism of methylene blue by graphene oxide-shielded Mg–Al-layered double hydroxide from synthetic wastewater, J. Phys. Chem. A 125 (4) (2021) 954–965.

[84] T.-D. Nguyen-Phan, et al., The role of graphene oxide content on the adsorption-enhanced photocatalysis of titanium dioxide/graphene oxide composites, Chem. Eng. J. 170 (1) (2011) 226–232.

[85] F. Wang, et al., Fe3O4@ SiO2@ CS-TETA functionalized graphene oxide for the adsorption of methylene blue (MB) and Cu (II), Appl. Surf. Sci. 420 (2017) 970–981.

[86] L. Zhang, et al., Facile construction of dual functional Fe3O4@ C-MoO2-Ni composites for catalysis and adsorption, Appl. Surf. Sci. 494 (2019) 783–794.

[87] A.S. Tonge, et al., Coagulated mineral adsorbents for dye removal, and their process intensification using an agitated tubular reactor (ATR), ChemEngineering 5 (3) (2021) 35..

[88] A. Elsagh, et al., Evaluation of the potential cationic dye removal using adsorption by graphene and carbon nanotubes as adsorbents surfaces, Arab. J. Chem. 10 (2017) S2862–S2869.

[89] S.M. Al-Rashed, A.A. Al-Gaid, Kinetic and thermodynamic studies on the adsorption behavior of Rhodamine B dye on Duolite C-20 resin, J. Saudi Chem. Soc. 16 (2) (2012) 209–215.

[90] M.Y. Prajitno, et al., The effect of pre-activation and milling on improving natural clinoptilolite for ion exchange of cesium and strontium, J. Environ. Chem. Eng. 8 (1) (2020) 102991.

[91] S.P. Lee, et al., Flake size-dependent adsorption of graphene oxide aerogel, J. Mol. Liq. 277 (2019) 175–180.

[92] A. Arabpour, S. Dan, H. Hashemipour, Preparation and optimization of novel graphene oxide and adsorption isotherm study of methylene blue, Arab. J. Chem. 14 (3) (2021) 103003.

[93] G. McKay, G. Ramprasad, P. Pratapa Mowli, Equilibrium studies for the adsorption of dyestuffs from aqueous solutions by low-cost materials, Water Air Soil Pollut. 29 (3) (1986) 273–283.

[94] P. Bradder, et al., Dye adsorption on layered graphite oxide, J. Chem. Eng. Data 56 (1) (2011) 138–141.

[95] N. Ayawei, A.N. Ebelegi, D. Wankasi, Modelling and interpretation of adsorption isotherms, J. Chem. 2017 (2017) 3039817.

[96] M.A. Al-Ghouti, D.A. Da`ana, Guidelines for the use and interpretation of adsorption isotherm models: a review, J. Hazard. Mater. 393 (2020) 122383.

[97] J. Piekarski, K. Ignatowicz, T. Dąbrowski, Analysis of selected methods use for calculation of the coefficients of adsorption isotherms and simplified equations of adsorption dynamics with the use of IZO application, Materials (Basel, Switzerland) 14 (15) (2021) 4192.

[98] K.V. Kumar, K. Porkodi, Relation between some two-and three-parameter isotherm models for the sorption of methylene blue onto lemon peel, J. Hazard. Mater. 138 (3) (2006) 633–635.

[99] A. Dada, et al., Langmuir, Freundlich, Temkin and Dubinin–Radushkevich isotherms studies of equilibrium sorption of Zn2+ unto phosphoric acid modified rice husk, IOSR J. Appl. Chem. 3 (1) (2012) 38–45.

[100] S. Wang, Y. Boyjoo, A. Choueib, A comparative study of dye removal using fly ash treated by different methods, Chemosphere 60 (10) (2005) 1401–1407.

[101] R. Maryanti, et al., Adsorption of dye on carbon microparticles: physicochemical properties during adsorption, adsorption isotherm and education for students with special needs, Sains Malaysiana 49 (12) (2020) 2949–2960.

[102] Y. Li, et al., Comparative study of methylene blue dye adsorption onto activated carbon, graphene oxide, and carbon nanotubes, Chem. Eng. Res. Des. 91 (2) (2013) 361–368.

[103] W. Zhang, et al., Fast and considerable adsorption of methylene blue dye onto graphene oxide, Bull. Environ. Contam. Toxicol. 87 (1) (2011) 86.

[104] Y. Li, et al., Mechanical and dye adsorption properties of graphene oxide/chitosan composite fibers prepared by wet spinning, Carbohydr. Polym. 102 (2014) 755–761.

[105] S. Thangavel, G. Venugopal, Understanding the adsorption property of graphene-oxide with different degrees of oxidation levels, Powder Technol. 257 (2014) 141–148.

[106] C. Puri, G. Sumana, Highly effective adsorption of crystal violet dye from contaminated water using graphene oxide intercalated montmorillonite nanocomposite, Appl. Clay Sci. 166 (2018) 102–112.

[107] Z. Gan, X. Xing, Z. Xu, Effects of image charges, interfacial charge discreteness, and surface roughness on the zeta potential of spherical electric double layers, J. Chem. Phys. 137 (3) (2012) 034708.

[108] H. Sun, L. Cao, L. Lu, Magnetite/reduced graphene oxide nanocomposites: one step solvothermal synthesis and use as a novel platform for removal of dye pollutants, Nano Res. 4 (2011) 550–562.

[109] P. Sharma, et al., Kinetics and adsorption behavior of the methyl blue at the graphene oxide/reduced graphene oxide nanosheet–water interface: a comparative study, J. Chem. Eng. Data 58 (12) (2013) 3477–3488.

[110] C. Tang, et al., Comparison of the removal and adsorption mechanisms of cadmium and lead from aqueous solution by activated carbons prepared from Typha angustifolia and Salix matsudana, RSC Adv. 7 (26) (2017) 16092–16103.

[111] C.C. Nnaji, et al., Equilibrium and thermodynamic investigation of biosorption of nickel from water by activated carbon made from palm kernel chaff, Sci. Rep. 11 (1) (2021) 7808.

[112] B. Meroufel, et al., Adsorptive Removal of Anionic Dye from Aqueous Solutions by Algerian Kaolin: Characteristics, Isotherm, Kinetic and Thermodynamic Studies, 2013.

[113] L.K. de Assis, B.S. Damasceno, M.N. Carvalho, Oliveira EHC, M.G. Ghislandi, Adsorption capacity comparison between graphene oxide and graphene nanoplatelets for the removal of coloured textile dyes from wastewater, Environ. Technol. 41 (18) (2020) 2360–2371.

[114] D. Robati, et al., Removal of hazardous dyes-BR 12 and methyl orange using graphene oxide as an adsorbent from aqueous phase, Chem. Eng. J. 284 (2016) 687–697.

[115] Y. El Maguana, et al., Activated carbon for dyes removal: modeling and understanding the adsorption process, J. Chem. (2020) 2096834.

[116] P. Sirajudheen, et al., Effective removal of organic pollutants by adsorption onto chitosan supported graphene oxide-hydroxyapatite composite: a novel reusable adsorbent, J. Mol. Liq. 318 (2020) 114200.

[117] Y. Yildiz, et al., Highly monodisperse Pt/Rh nanoparticles confined in the graphene oxide for highly efficient and reusable sorbents for methylene blue removal from aqueous solutions, ChemistrySelect 2 (2) (2017) 697–701.

[118] K. Gul, et al., Removal of toxic malachite green dye from aqueous environment using reduced magnetic graphene oxide as an efficient and reusable adsorbent, Sep. Sci. Technol. 56 (15) (2021) 2507–2520.

[119] S. Azizkhani, et al., Synthesis and characterisation of graphene oxide-silica-chitosan for eliminating the Pb (II) from aqueous solution, Polymers 12 (9) (2020) 1922.

[120] X. Chen, et al., Adsorption of heavy metals by graphene oxide/cellulose hydrogel prepared from NaOH/urea aqueous solution, Materials 9 (7) (2016) 582.

[121] F. Ren, et al., Facile preparation of 3D regenerated cellulose/graphene oxide composite aerogel with high-efficiency adsorption towards methylene blue, J. Colloid Interface Sci. 532 (2018) 58–67.

[122] F. Shoushtarian, M.R.A. Moghaddam, E. Kowsari, Efficient regeneration/reuse of graphene oxide as a nanoadsorbent for removing basic red 46 from aqueous solutions, J. Mol. Liq. 312 (2020) 113386.

[123] V. Dolia, et al., Dissimilar adsorption of higher-order aggregates compared with monomers and dimers of methylene blue on graphene oxide: an optical spectroscopic perspective, Carbon Trends 4 (2021) 100066.

[124] S. Jayanthi, et al., Macroporous three-dimensional graphene oxide foams for dye adsorption and antibacterial applications, RSC Adv. 6 (2) (2016) 1231–1242.

[125] M. Nagpal, R. Kakkar, Facile synthesis of mesoporous magnesium oxide–graphene oxide composite for efficient and highly selective adsorption of hazardous anionic dyes, Res. Chem. Intermed. 46 (5) (2020) 2497–2521.

[126] I. Chowdhury, et al., Colloidal properties and stability of graphene oxide nanomaterials in the aquatic environment, Environ. Sci. Technol. 47 (12) (2013) 6288–6296.

[127] E.R. Smith, Experiments in Light Scattering: Examining Aqueous Suspensions of Graphene Oxide and the Aggregation Behavior of Bordeaux Dye, 2010.

[128] Y. Yue, et al., Preparation of an anti-aggregation silica/zinc/graphene oxide nanocomposite with enhanced adsorption capacity 25 (71) (2019) 16340–16349.

[129] S.-C. Wu, et al., Synthesis of aluminum-based MOF/graphite oxide composite and enhanced removal of methyl orange, J. Alloys Compd. 724 (2017) 625–632.

[130] W. Peng, et al., Adsorption of methylene blue on graphene oxide prepared from amorphous graphite: effects of pH and foreign ions, J. Mol. Liq. 221 (2016) 82–87.

[131] S. Chowdhury, R. Balasubramanian, Recent advances in the use of graphene-family nanoadsorbents for removal of toxic pollutants from wastewater, Adv. Colloid Interf. Sci. 204 (2014) 35–56.

[132] H. Kim, et al., Adsorption isotherms and kinetics of cationic and anionic dyes on three-dimensional reduced graphene oxide macrostructure, J. Ind. Eng. Chem. 21 (2015) 1191–1196.

[133] A. Doi, et al., Specificity and affinity of multivalent ions adsorption to kaolinite surface, Appl. Clay Sci. 190 (2020) 105557.

[134] M. Alkan, Ö. Demirbaş, M. Doğan, Electrokinetic properties of sepiolite suspensions in different electrolyte media, J. Colloid Interface Sci. 281 (1) (2005) 240–248.

[135] K. Yang, et al., Aggregation, adsorption, and morphological transformation of graphene oxide in aqueous solutions containing different metal cations, Environ. Sci. Technol. 50 (20) (2016) 11066–11075.